Computational mean-field modeling of confined active fluids

Maxime Theillard [a,*], David Saintillan [b]

[a] *School of Natural Sciences, Applied Mathematics Unit, University of California, Merced, CA 95340, USA*
[b] *Department of Mechanical and Aerospace Engineering, University of California San Diego, 9500 Gilman Drive, La Jolla CA 92093, USA*

ABSTRACT

We present a new framework for the efficient simulation of the dynamics of active fluids in complex two- and three-dimensional microfluidic geometries. Focusing on the case of a suspension of microswimmers such as motile bacteria, we adopt a continuum mean-field model based on partial differential equations for the evolution of the concentration, polarization and nematic tensor fields, which are nonlinearly coupled to the Navier-Stokes equations for the fluid flow driven by internal active stresses. A level set method combined with an adaptive mesh refinement scheme on Quad-/Octree grids is used to capture complex domain shapes while refining the solution near boundaries or in the neighborhood of sharp gradients. A hybrid finite volumes/finite differences method is implemented in which the concentration field is treated using finite volumes to ensure mass conservation, while the polarization and nematic alignment fields are treated using a combination of finite differences and finite volumes for enhanced accuracy. The governing equations for these fields are solved along with the Navier-Stokes equations, which are evolved using an unconditionally stable projection solver. We illustrate the versatility and robustness of our method by analyzing spontaneous active flows in various two- and three-dimensional systems. Our results show excellent agreement with previous models and experiments and pave the way for further developments in active microfluidics.

Published by Elsevier Inc.

1. Introduction

The fast-growing field of active matter has excited physicists and engineers alike, providing both a wealth of emergent phenomena to be elucidated and the potential for novel technological applications that harness the internal energy production unique to these materials. Many active matter systems consist of collections of particles, cells, or macromolecules (e.g., autophoretic colloids [40], swimming microorganisms [25], or microtubules/kinesin clusters [53]) suspended in a viscous fluid that mediates hydrodynamic interactions resulting from active stresses exerted on the microscale [20,44,45]. A peculiar feature of these systems is their ability to self-organize and exhibit spontaneously flowing states on mesoscopic length scales [24,33], which take the form of chaotic turbulent-like motions in bulk systems [60,52] and of steady unidirectional flows in confined geometries [64,63,32,61,65]. The transitions toward these states are thought to be caused by hydrodynamic instabilities driven internally by active stresses [48,54,4,15,59], and are also closely connected to the unusual rheology of these materials [45].

Numerical simulations have played a central role in the investigation of active fluids, allowing one to probe the microscopic mechanisms underlying experimentally observed dynamics. Direct particle simulations of systems such as mi-

croswimmer suspensions [21,47,46,12] and active nematic liquid crystals [18] have been useful for the study of dynamics on small scales, providing detailed information about the local microstructure. Another approach has been based on continuum kinetic models [33,50], which coarse-grain interparticle and hydrodynamic interactions into systems of mean-field partial differential equations coupling microstructural variables with the underlying fluid motion. In a popular class of models [48,4,54], a Smoluchowski equation for the distribution function $\Psi(\mathbf{x}, \mathbf{p}, t)$ of particles with position $\mathbf{x}$ and orientation $\mathbf{p}$ is solved along with the Navier-Stokes equations with a volumetric body force deriving from an active stress tensor. The high-dimensionality of the problem and complexity of boundary conditions, however, have restricted simulations to simple geometries [49,15]. The model can be further reduced by deriving equations for the orientational moments of the distribution function, such as the concentration $c(\mathbf{x}, t)$, polarization vector $\mathbf{m}(\mathbf{x}, t)$ and nematic tensor $\mathbf{D}(\mathbf{x}, t)$, which have simple interpretations and are useful descriptors of the microstructure. These variables satisfy a hierarchy of coupled partial differential equations requiring a closure approximation, such as a near-isotropy closure scheme [4,50,55] or the more sophisticated Bingham closure [17]. The resulting set of equations is more easily solved numerically, and recent simulations in various simple geometries have provided valuable insight into instabilities and nonlinear dynamics [17,55,6].

Simulations in complex geometries, especially in three dimensions, have been scarce. The difficulty has stemmed in part from the multiscale nature of the problem, which requires resolving microstructural boundary layers near surfaces as well as complex flow dynamics. In microswimmer suspensions, the tendency of particles to accumulate at boundaries indeed results in sharp gradients [14] and also requires numerical schemes with good conservation properties to avoid mass losses. Away from boundaries, turbulent-like dynamics result in unsteady velocity and microstructural gradients on a wide range of length scales set by the range of unstable modes allowed in a particular geometry. Here, we present a simulation framework that overcomes these challenges while enabling efficient simulations in complex two- and three-dimensional geometries. We focus on the case of a suspension of microswimmers such as motile bacteria and adopt a continuum model based on orientational moments used in our previous work [55]. A level set method combined with an adaptive mesh refinement scheme on Quad-/Octrees [36] is used to capture complex domain shapes while refining the solution near boundaries or in the vicinity of sharp gradients. A hybrid finite volumes/differences method is implemented in which the concentration field is treated using finite volumes to ensure mass conservation while the polarization and nematic tensor fields are treated using a combination of finite differences and finite volumes for enhanced accuracy [56]. The evolution equations for these fields are coupled to the Navier-Stokes equations for the fluid motion, which are evolved using an unconditionally stable projection solver [19]. This novel method was applied to study spontaneous active flows in two dimensional systems in our recent work [55], where the results were analyzed in detail and shown to reproduce experimental observations in microfluidic systems. The present paper provides a detailed account of the numerical method used in [55] and extends it to three spatial dimensions. The method, whose robustness and versatility are illustrated in various examples, provides a unique tool for studying active fluid flows in complex geometries and paves the way for new developments in computational active microfluidics.

The paper is organized as follows. We present the governing equations for the evolution of the microstructure and fluid flow along with their non-dimensionalized versions in section 2. The semi-implicit scheme and functional iterations used for time-marching are described in section 3. The level set method and grid generation procedure are explained in sections 4 and 5, followed by a detailed account of the finite volume/difference approximations used for spatial discretizations in section 6. We then validate and illustrate our method on various 2D and 3D examples motivated by existing experimental observations in section 7, and we conclude in section 8.

2. Governing equations

2.1. Continuum mean-field model

We employ a continuum model for active suspensions first developed by Saintillan & Shelley [48,49] and subsequently applied to study active collective motions in bulk [15] as well as confined systems [55]. We consider a suspension of active Brownian swimmers with mean number density n confined in a domain Ω with fixed boundary $\partial\Omega$ and characteristic size H. The swimmers self-propel with constant velocity V_s along their unit director $\mathbf{p}$ and have constant translational and rotational diffusivities d_t and d_r, respectively. As they swim, they exert a net symmetric force dipole on the suspending fluid with stresslet strength σ_0 [20,45]. The suspending fluid is assumed to be Newtonian and incompressible with density ρ and dynamic viscosity μ.

To describe the configuration and dynamics of the suspension we employ a continuum mean-field approach based on the probability density function $\Psi(\mathbf{x}, \mathbf{p}, t)$ of finding a swimmer at position $\mathbf{x}$ with orientation $\mathbf{p}$ at time t. Following [49], the evolution of Ψ is captured by a Smoluchowski equation

$$\partial_t \Psi + \nabla_x \cdot (\dot{\mathbf{x}}\Psi) + \nabla_p \cdot (\dot{\mathbf{p}}\Psi) = 0 \qquad \forall (\mathbf{x}, \mathbf{p}) \in \Omega \times C, \tag{1}$$

where ∇_x and ∇_p are the spatial and orientational gradient operators, Ω is the domain occupied by the suspension, and C is the space of orientations, which is the unit circle in 2D and the unit sphere in 3D. The translational flux velocity $\dot{\mathbf{x}}$ is modeled as

$$\dot{\mathbf{x}} = V_s \mathbf{p} + \mathbf{u} - d_t \nabla_x \ln \Psi, \tag{2}$$

and accounts for self propulsion of the swimmers, advection by the mean-field background flow $\mathbf{u}$ and translational diffusion. The orientational flux velocity $\dot{\mathbf{p}}$ is similarly expressed as

$$\dot{\mathbf{p}} = (\mathbf{I} - \mathbf{pp}) \cdot (\zeta \mathbf{E} - \mathbf{W}) \cdot \mathbf{p} - d_r \nabla_p \ln \Psi, \tag{3}$$

and accounts for reorientation of the swimmers by the local rate-of-strain and vorticity tensors $\mathbf{E} = \frac{1}{2}(\nabla \mathbf{u} + \nabla \mathbf{u}^T)$ and $\mathbf{W} = \frac{1}{2}(\nabla \mathbf{u} - \nabla \mathbf{u}^T)$ as well as rotational diffusion. The first term on the right-hand side is the celebrated Jeffery's equation [23], where the dimensionless parameter ζ is known as Bretherton's constant and characterizes particle shape [5], with $\zeta = 0$ for spheres such as self-propelled colloids and $\zeta \approx 1$ for slender particles such as bacteria. On the confining boundary $\partial \Omega$, a no-flux condition is prescribed on the probability density function [14]:

$$\mathbf{n} \cdot \dot{\mathbf{x}} = 0 \qquad \forall (\mathbf{x}, \mathbf{p}) \in \partial \Omega \times C, \tag{4}$$

which ensures that the total number of swimmers in the system is conserved.

2.2. Dimensional analysis

Using H as length scale and d_r^{-1} as time scale, non-dimensionalization of the governing equations yields the four dimensionless groups

$$Pe_s = \frac{V_s}{d_r H}, \qquad \alpha = \frac{\sigma_0 n}{\mu d_r}, \qquad \Lambda = \frac{d_r d_t}{V_s^2}, \qquad Re = \frac{\rho H^2 d_r}{\mu}. \tag{5}$$

The swimming Péclet number Pe_s denotes the ratio of the persistence length of swimmer trajectories to the characteristic size of the domain and is a measure of confinement. The parameter α compares the effect of active stresses exerted by the swimmers on the fluid to the dissipative effects of viscosity and rotational diffusion. It is a signed coefficient that depends on the type of swimmer [45]: $\alpha < 0$ for so-called *pushers* such as bacteria that exert a thrust with their flagellar tail [8], and $\alpha > 0$ for so-called *pullers* such as certain micro-algae that exert a thrust with their anterior flagella [9]. Past studies have shown that collective motion typically arises in sufficiently dense suspensions of pushers [49,46], which can be rationalized theoretically using a stability analysis or based on arguments on the system's configurational entropy [49,22]. The parameter Λ is swimmer-specific and compares the strength of propulsion to Brownian diffusion; the limit $\Lambda \to 0$ describes purely ballistic swimmers, while $\Lambda \to \infty$ corresponds to purely diffusive swimmers. Finally, Re denotes the Reynolds number, which is typically small in active suspensions. We henceforth exclusively use dimensionless variables and equations.

2.3. Orientational moments and closure approximation

Solving the Smoluchowski equation directly, while possible in simple geometries [49,14], is computationally challenging and expensive due to the high dimensionality of the problem. Instead, it is possible to reduce the dimensionality by using a closure approximation that expresses the probability density function Ψ in terms of its orientational moments [50]. In 2D, we use the approximation

$$\Psi(\mathbf{x}, \mathbf{p}, t) \approx \frac{1}{2\pi} \Big(c(\mathbf{x}, t) + 2\mathbf{p} \cdot \mathbf{m}(\mathbf{x}, t) + 4\mathbf{pp} : \mathbf{D}(\mathbf{x}, t) \Big), \tag{6}$$

which can be interpreted as a truncated Fourier series expansion; corresponding expressions in 3D are provided in section 2.6. The moments c, $\mathbf{m}$, and $\mathbf{D}$, which no longer depend on $\mathbf{p}$, are defined as integrals over the unit circle C of orientations:

$$c(\mathbf{x}, t) = \int_C \Psi(\mathbf{x}, \mathbf{p}, t) \, d\mathbf{p}, \tag{7}$$

$$\mathbf{m}(\mathbf{x}, t) = \int_C \mathbf{p} \, \Psi(\mathbf{x}, \mathbf{p}, t) \, d\mathbf{p}, \tag{8}$$

$$\mathbf{D}(\mathbf{x}, t) = \int_C \left(\mathbf{pp} - \frac{\mathbf{I}}{2} \right) \Psi(\mathbf{x}, \mathbf{p}, t) \, d\mathbf{p}. \tag{9}$$

The zeroth-order moment c denotes the local particle concentration. The first-order moment $\mathbf{m}$ is known as the polarization and captures the mean direction of swimming. Finally, the second-order moment $\mathbf{D}$ is the nematic alignment tensor, which in the current form is symmetric and trace-free and describes local particle alignment irrespective of swimming direction. Evolution equations for these three quantities can be obtained by taking orientational moments of the Smoluchovski Eq. (1) and are given by

$$\partial_t c = -\nabla \cdot \mathbf{F}_c, \tag{10}$$

$$\partial_t \mathbf{m} = -\nabla \cdot \mathbf{F}_m + \mathbf{H}_m - \mathbf{m}, \tag{11}$$

$$\partial_t \mathbf{D} = -\nabla \cdot \mathbf{F}_D + \mathbf{H}_D - 4\mathbf{D}, \tag{12}$$

where the translational fluxes are

$$\mathbf{F}_c = \mathbf{u}\,c + Pe_s\,\mathbf{m} - \Lambda Pe_s^2 \nabla c, \tag{13}$$

$$\mathbf{F}_m = \mathbf{u}\,\mathbf{m} + Pe_s\left(\mathbf{D} + c\frac{\mathbf{I}}{2}\right) - \Lambda Pe_s^2 \nabla \mathbf{m}, \tag{14}$$

$$\mathbf{F}_D = \mathbf{u}\,\mathbf{D} + Pe_s\left(\mathbf{T} - \mathbf{m}\frac{\mathbf{I}}{2}\right) - \Lambda Pe_s^2 \nabla \mathbf{D}, \tag{15}$$

and the source terms $\mathbf{H}_m$ and $\mathbf{H}_D$ come from Jeffery's equation and describe particle alignment by the flow:

$$\mathbf{H}_m = \tfrac{1}{2}\zeta \mathbf{E} \cdot \mathbf{m} - \mathbf{W} \cdot \mathbf{m}, \tag{16}$$

$$\mathbf{H}_D = \tfrac{1}{2}\zeta c\mathbf{E} + \tfrac{2}{3}\zeta \mathbf{E} \cdot \mathbf{D} - \tfrac{1}{3}\zeta (\mathbf{D} : \mathbf{E})\mathbf{I} + \mathbf{D} \cdot \mathbf{W} - \mathbf{W} \cdot \mathbf{D}. \tag{17}$$

The flux for $\mathbf{D}$ in Eq. (15) involves the third-order orientational moment $\mathbf{T}$. Based on the closure approximation implied by Eq. (6), it can be related to the polarization as

$$T_{ijk} = \tfrac{1}{4}\left(m_i\delta_{jk} + m_j\delta_{ik} + m_k\delta_{ij}\right). \tag{18}$$

Taking the first three moments of the boundary condition Eq. (4) yields no-flux conditions for the moments at the domain boundary:

$$\mathbf{n} \cdot \mathbf{F}_c = \mathbf{n} \cdot \mathbf{F}_m = \mathbf{n} \cdot \mathbf{F}_D = 0 \qquad \forall \mathbf{x} \in \partial\Omega. \tag{19}$$

2.4. Fluid motion

We assume that the suspending fluid is Newtonian and that the flow is incompressible, so that the velocity and pressure fields satisfy the incompressible Navier-Stokes equations:

$$Re\left(\partial_t \mathbf{u} + \mathbf{u} \cdot \nabla \mathbf{u}\right) = -\nabla p + \nabla \cdot (\nabla \mathbf{u} + \alpha \mathbf{D}) \qquad \forall \mathbf{x} \in \Omega, \tag{20}$$

$$\nabla \cdot \mathbf{u} = 0, \tag{21}$$

supplemented by the no-slip condition on the boundary

$$\mathbf{u} = 0 \qquad \forall \mathbf{x} \in \partial\Omega. \tag{22}$$

In Eq. (20), the last term involves the active stress tensor $\alpha\mathbf{D}$, which captures the effect of the force dipoles exerted by the swimmers on the fluid as they self-propel [20,45].

2.5. Summary of the governing equations

Using incompressibility, we rewrite the coupled non-linear equations Eqs. (10), (11), (12), (20), and (21) capturing the dynamics of the suspension and fluid motion inside the domain Ω as

$$\partial_t c + \mathbf{u} \cdot \nabla c = \Lambda Pe_s^2 \Delta c - Pe_s \nabla \cdot \mathbf{m}, \tag{23}$$

$$\partial_t \mathbf{m} + \mathbf{u} \cdot \nabla \mathbf{m} = \Lambda Pe_s^2 \Delta \mathbf{m} - \mathbf{m} - Pe_s \nabla \cdot \left(\mathbf{D} + c\frac{\mathbf{I}}{2}\right) + \mathbf{H}_m, \tag{24}$$

$$\partial_t \mathbf{D} + \mathbf{u} \cdot \nabla \mathbf{D} = \Lambda Pe_s^2 \Delta \mathbf{D} - 4\mathbf{D} - Pe_s \nabla \cdot \left(\mathbf{T} - \mathbf{m}\frac{\mathbf{I}}{2}\right) + \mathbf{H}_D, \tag{25}$$

$$Re\left(\partial_t \mathbf{u} + \mathbf{u} \cdot \nabla \mathbf{u}\right) = -\nabla p + \Delta \mathbf{u} + \alpha \nabla \cdot \mathbf{D}, \tag{26}$$

$$\nabla \cdot \mathbf{u} = 0. \tag{27}$$

Boundary conditions (13), (14), and (15) for the moments, combined with the no-slip condition $\mathbf{u} = \mathbf{0}$ on $\partial\Omega$, yield the Neumann-like boundary conditions

$$\Lambda Pe_s \mathbf{n} \cdot \nabla c = \mathbf{n} \cdot \mathbf{m}, \tag{28}$$

$$\Lambda Pe_s \mathbf{n} \cdot \nabla \mathbf{m} = \mathbf{n} \cdot \left(\mathbf{D} + c\frac{\mathbf{I}}{2}\right), \tag{29}$$

$$\Lambda Pe_s \mathbf{n} \cdot \nabla \mathbf{D} = \mathbf{n} \cdot \left(\mathbf{T} - \mathbf{m}\frac{\mathbf{I}}{2}\right). \tag{30}$$

The above system of coupled non-linear partial differential equations and boundary conditions constitutes a complete system governing the coupled evolution of swimmer configurations and suspending fluid flow.

Some of the basic physics of active suspensions can be gleaned from the various couplings dictated by these governing equations. The generic instability of pusher suspensions [48], which results in spontaneous chaotic flows in bulk systems, is rooted in the active stress tensor $\alpha \mathbf{D}$ that forces the Navier-Stokes equations: in suspensions of pushers ($\alpha < 0$), perturbations in nematic alignment drive flows through the active forcing term, which in turn reinforces the nematic alignment via the nonlinear source term $\mathbf{H}_D$ in equation (26). This feedback loop, which results in the growth of nematic bend fluctuations, has been analyzed in detail in the past using linearized stability theories [48,49,15,4,54]. In suspensions of swimmers, nematic alignment combined with self-propulsion also results in polarization via the term $Pe_s \nabla \cdot \mathbf{D}$ in equation (25), which is ultimately responsible for concentration fluctuations via the term $Pe_s \nabla \cdot \mathbf{m}$ in equation (23).

2.6. Governing equations in three dimensions

In three spatial dimensions, the governing equations can be obtained through the same methodology. The equations retain the same structure with slightly different coefficients, which result from new expressions for the nematic tensor and for the third-moment closure:

$$\mathbf{D}(\mathbf{x}, t) = \int_C \left(\mathbf{pp} - \frac{\mathbf{I}}{3} \right) \Psi(\mathbf{x}, \mathbf{p}, t) \, d\mathbf{p}, \tag{31}$$

$$T_{ijk} = \tfrac{1}{5} \left(m_i \delta_{jk} + m_j \delta_{ik} + m_k \delta_{ij} \right). \tag{32}$$

Governing equations for the concentration field and fluid flow are unaffected by these new definitions and remain identical to Eqs. (23), (26), and (27). The evolution equations for the polarization and nematic tensor become

$$\partial_t \mathbf{m} + \mathbf{u} \cdot \nabla \mathbf{m} = \Lambda Pe_s^2 \Delta \mathbf{m} - 2\mathbf{m} - Pe_s \nabla \cdot \left(\mathbf{D} + c\frac{\mathbf{I}}{3} \right) + \mathbf{H}_m, \tag{33}$$

$$\partial_t \mathbf{D} + \mathbf{u} \cdot \nabla \mathbf{D} = \Lambda Pe_s^2 \Delta \mathbf{D} - 6\mathbf{D} - Pe_s \nabla \cdot \left(\mathbf{T} - \mathbf{m}\frac{\mathbf{I}}{3} \right) + \mathbf{H}_D, \tag{34}$$

where hydrodynamic coupling terms are now expressed as

$$\mathbf{H}_m = \tfrac{3}{5} \zeta \mathbf{E} \cdot \mathbf{m} - \mathbf{W} \cdot \mathbf{m}, \tag{35}$$

$$\mathbf{H}_D = \tfrac{2}{5} \zeta c \mathbf{E} + \tfrac{6}{7} \zeta \mathbf{E} \cdot \mathbf{D} - \tfrac{2}{7} \zeta (\mathbf{D} : \mathbf{E})\mathbf{I} + \mathbf{D} \cdot \mathbf{W} - \mathbf{W} \cdot \mathbf{D}. \tag{36}$$

3. Time discretization

3.1. Semi-implicit scheme

Our numerical approach is constructed as a variable-time-step semi-implicit method, where advective terms are treated using a Semi-Lagrangian Backward Difference (SLBDF) scheme [34,19], while all other terms, including the right-hand sides of the boundary conditions (28), (29) and (30), are treated implicitly. Specifically,

$$\beta c^{n+1} + \gamma c_d^n + \delta c_d^{n-1} = \Lambda Pe_s^2 \Delta c^{n+1} - Pe_s \nabla \cdot \mathbf{m}^{n+1}, \tag{37}$$

$$\beta \mathbf{m}^{n+1} + \gamma \mathbf{m}_d^n + \delta \mathbf{m}_d^{n-1} = \Lambda Pe_s^2 \Delta \mathbf{m}^{n+1} - \mathbf{m}^{n+1} - Pe_s \nabla \cdot \left(\mathbf{D} + c\frac{\mathbf{I}}{2} \right)^{n+1} + \mathbf{H}_m^{n+1}, \tag{38}$$

$$\beta \mathbf{D}^{n+1} + \gamma \mathbf{D}_d^n + \delta \mathbf{D}_d^{n-1} = \Lambda Pe_s^2 \Delta \mathbf{D}^{n+1} - 4\mathbf{D}^{n+1} - Pe_s \nabla \cdot \left(\mathbf{T} - \mathbf{m}\frac{\mathbf{I}}{2} \right)^{n+1} + \mathbf{H}_D^{n+1}, \tag{39}$$

$$Re \left(\beta \mathbf{u}^{n+1} + \gamma \mathbf{u}_d^n + \delta \mathbf{u}_d^{n-1} \right) = -\nabla p^{n+1} + \Delta \mathbf{u}^{n+1} + \alpha \nabla \cdot \mathbf{D}^{n+1}, \tag{40}$$

$$\nabla \cdot \mathbf{u}^{n+1} = 0, \tag{41}$$

with boundary conditions on $\partial \Omega$ given by

$$\Lambda Pe_s \mathbf{n} \cdot \nabla c^{n+1} = \mathbf{n} \cdot \mathbf{m}^{n+1}, \tag{42}$$

$$\Lambda Pe_s \mathbf{n} \cdot \nabla \mathbf{m}^{n+1} = \mathbf{n} \cdot \left(\mathbf{D} + c\frac{\mathbf{I}}{2} \right)^{n+1}, \tag{43}$$

$$\Lambda Pe_s \mathbf{n} \cdot \nabla \mathbf{D}^{n+1} = \mathbf{n} \cdot \left(\mathbf{T} - \mathbf{m}\frac{\mathbf{I}}{2} \right)^{n+1}, \tag{44}$$

$$\mathbf{u}^{n+1} = \mathbf{0}. \tag{45}$$

The time-step-dependent coefficients β, γ, δ in Eqs. (37)–(40) are given by

$$\beta = \frac{2\Delta t_n + \Delta t_{n-1}}{\Delta t_n(\Delta t_n + \Delta t_{n-1})}, \qquad \delta = \frac{\Delta t_n}{\Delta t_{n-1}(\Delta t_n + \Delta t_{n-1})}, \qquad \gamma = -\beta - \delta. \tag{46}$$

The variables identified by subscript d are estimated at time steps t_n and t_{n-1} and at the departure points x_d^n, x_d^{n-1} from which the characteristic curves originate, e.g., $c_d^n = c(\mathbf{x}_d^n, t^n)$, $c_d^{n-1} = c(\mathbf{x}_d^{n-1}, t^{n+1})$. The departure points are determined using a second-order modified explicit mid-point scheme:

$$\mathbf{x}^* = \mathbf{x}^{n+1} - \frac{\Delta t_n}{2}\mathbf{u}^n(\mathbf{x}^{n+1}), \tag{47}$$

$$\mathbf{u}^* = \left(1 + \frac{\Delta t_n}{2\Delta t_{n-1}}\right)\mathbf{u}^n(\mathbf{x}^*) - \frac{\Delta t_n}{2\Delta t_{n-1}}\mathbf{u}^{n-1}(\mathbf{x}^*), \tag{48}$$

$$\mathbf{x}_d^n = \mathbf{x}^{n+1} - \Delta t_n\mathbf{u}^*, \tag{49}$$

and

$$\mathbf{x}^* = \mathbf{x}^{n+1} - \Delta t_n\mathbf{u}^n(\mathbf{x}^{n+1}), \tag{50}$$

$$\mathbf{u}^* = \mathbf{u}^n(\mathbf{x}^*), \tag{51}$$

$$\mathbf{x}_d^{n-1} = \mathbf{x}^{n+1} - (\Delta t_n + \Delta t_{n-1})\,\mathbf{u}^*. \tag{52}$$

The velocities $\mathbf{u}^n(\mathbf{x}^*)$ and $\mathbf{u}^{n-1}(\mathbf{x}^*)$ at the mid-points as well as various quantities at the departing points such as c_d^{n-1} and c_d^n are approximated using third-order-accurate interpolation. This temporal discretization ensures that the overall method is unconditionally strongly stable, with an accuracy in time that is determined by the accuracy of the semi-Lagrangian method.

3.2. Functional iterations

We employ an iterative method to address the non-linearity incurred by hydrodynamic interactions in Eqs. (16)–(17). At each time step t_n, we compute the next solution at time t_{n+1} iteratively and initialize it with the solution at the previous time step:

$$c_0^{n+1} = c^n, \qquad \mathbf{m}_0^{n+1} = \mathbf{m}^n, \qquad \mathbf{D}_0^{n+1} = \mathbf{D}^n, \qquad \mathbf{u}_0^{n+1} = \mathbf{u}^n, \tag{53}$$

where subscript $k = 0$ refers to iteration number. We then correct it iteratively using implicit correctors and the latest available solution corrections to calculate nonlinear coupling terms. We start by computing the new concentration field c_{k+1}^{n+1} as the solution of the following Poisson problem obtained from Eq. (37) with a Neumann boundary condition on $\partial\Omega$ obtained from Eq. (42):

$$\left(\beta\mathbf{I} - \Lambda Pe_s^2\Delta\right)c_{k+1}^{n+1} = -\gamma c_d^n - \delta c_d^{n-1} - Pe_s\nabla\cdot\mathbf{m}_k^{n+1} \qquad \forall\mathbf{x}\in\Omega, \tag{54}$$

$$\Lambda Pe_s\mathbf{n}\cdot\nabla c_{k+1}^{n+1} = \mathbf{n}\cdot\mathbf{m}_k^{n+1} \qquad \forall\mathbf{x}\in\partial\Omega. \tag{55}$$

The new values of the polarization field $\mathbf{m}_{k+1}^{n+1}$ and nematic tensor $\mathbf{D}_{k+1}^{n+1}$ are then obtained, respectively, by solving the two problems

$$\left((1+\beta)\mathbf{I} - \Lambda Pe_s^2\Delta\right)\mathbf{m}_{k+1}^{n+1} = -\gamma\mathbf{m}_d^n - \delta\mathbf{m}_d^{n-1} - Pe_s\nabla\cdot\left(\mathbf{D}_k^{n+1} + c_{k+1}^{n+1}\frac{\mathbf{I}}{2}\right) + \mathbf{H}_{m,k}^{n+1} \qquad \forall\mathbf{x}\in\Omega, \tag{56}$$

$$\Lambda Pe_s\mathbf{n}\cdot\nabla\mathbf{m}_{k+1}^{n+1} = \mathbf{n}\cdot\left(\mathbf{D}_k^{n+1} + c_{k+1}^{n+1}\frac{\mathbf{I}}{2}\right) \qquad \forall\mathbf{x}\in\partial\Omega, \tag{57}$$

and

$$\left((4+\beta)\mathbf{I} - \Lambda Pe_s^2\Delta\right)\mathbf{D}_{k+1}^{n+1} = -\gamma\mathbf{D}_d^n - \delta\mathbf{D}_d^{n-1} - Pe_s\nabla\cdot\left(\mathbf{T}_{k+1}^{n+1} - \mathbf{m}_{k+1}^{n+1}\frac{\mathbf{I}}{2}\right) + \mathbf{H}_{D,k}^{n+1} \qquad \forall\mathbf{x}\in\Omega, \tag{58}$$

$$\Lambda Pe_s\mathbf{n}\cdot\nabla\mathbf{D}_{k+1}^{n+1} = \mathbf{n}\cdot\left(\mathbf{T}_{k+1}^{n+1} - \mathbf{m}_{k+1}^{n+1}\frac{\mathbf{I}}{2}\right) \qquad \forall\mathbf{x}\in\partial\Omega. \tag{59}$$

We then compute the active fluid forcing $\alpha\nabla\cdot\mathbf{D}_{k+1}^{n+1}$ and use it to update the fluid velocity based on Eqs. (40)–(41) subject to the no-slip condition (22).

The iterative process terminates when the relative variations between two consecutive corrections of the concentration field are less than an arbitrary error tolerance

$$\frac{||c_{k+1}^{n+1} - c_k^{n+1}||_\infty}{||c_{k+1}^{n+1}||_\infty} < \epsilon, \tag{60}$$
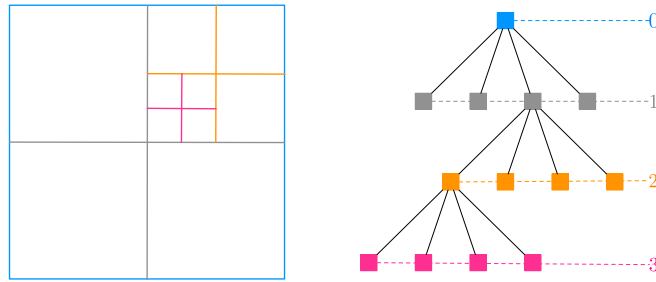
Fig. 1. Quadtree construction and tree representation. Starting from the root cell (blue) representing the entire computational domain, the mesh is recursively adapted according to criteria (65) and (66). The level of a cell is defined as the number of splits needed to produce it. (For interpretation of the colors in the figure(s), the reader is referred to the web version of this article.)

which we set to $\epsilon = 10^{-6}$. It is clear from the above formulation that the process, if it converges, must yield the desired solution. Our numerical experiments suggest that the method converges exponentially fast with the number of iterations, which is unsurprising due to the structure of Eqs. (54), (56) and (58), which are Poisson-like problems with extra diagonal coefficients. Once convergence has been achieved, the solution is updated, the mesh and time step are adapted based on the new solution, and all quantities are interpolated to the new mesh.

4. Implicit geometric representation: level set method

We employ the level set method to describe the confining domain geometry $\partial \Omega$, which is represented implicitly by the zero contour of a level set function ϕ [42] such that

$$\phi(\mathbf{x}) = 0 \qquad \forall \mathbf{x} \in \partial \Omega, \tag{61}$$

$$\phi(\mathbf{x}) \leq 0 \qquad \forall \mathbf{x} \in \Omega. \tag{62}$$

For numerical stability reasons, we impose it to be a signed distance function:

$$|\nabla \phi| = 1 \qquad \forall \mathbf{x} \in \Omega. \tag{63}$$

In practice, the level set function is generated at the very beginning of the algorithm, is reinitialized using a Total Variation Diminishing second-order Runge-Kutta method [36], and an original copy is stored aside. At each time step, after the mesh has been updated, a copy of the original level set is interpolated at the nodes of the new mesh and reinitialized to satisfy $|\nabla \phi| = 1$ since interpolation does not preserve this condition. This copy is then used to compute the various solutions at the new time step. Both the value of the level set function (signed distance to the interface) and its normalized gradient

$$\frac{\nabla \phi}{|\nabla \phi|} = \mathbf{n} \tag{64}$$

are needed by the algorithm.

5. Quadtree grids

5.1. Tree construction and refinement strategy

In two dimensions, the computational domain is discretized using a Quadtree grid [51], which we continuously adapt to the geometry and solution. As illustrated in Fig. 1, the grid is constructed starting from a single cell (the root of the tree, level 0) corresponding to the entire computational domain, which we subdivide into four identical daughter cells (level 1). We then decide based on a refinement criterion to be specified later whether to further subdivide each of these cells into four identical cells (level 2). The procedure is recursively applied to the newly created cells until a termination criterion is attained. Formally, we define the level of a cell as the number of subdivisions required to create it, and denote by $\min_{\text{level}}$ and $\max_{\text{level}}$ the minimum and maximum refinement levels of the tree, respectively.

We employ two distinct refinement criteria based on geometry and on spatial variations of the desired solution. First, to ensure that the mesh is refined at its maximum resolution close to the domain boundaries [36] and has a prescribed minimum level $\min_{\text{level}}$, we split any cell C if

$$\text{level}(C) < \min_{\text{level}}, \quad \text{or} \quad \min_{v \in \text{nodes}(C)} |\phi(v)| \leq \text{Lip}(\phi)\text{diag}(C) \quad \text{and} \quad \text{level}(C) < \max_{\text{level}}, \tag{65}$$
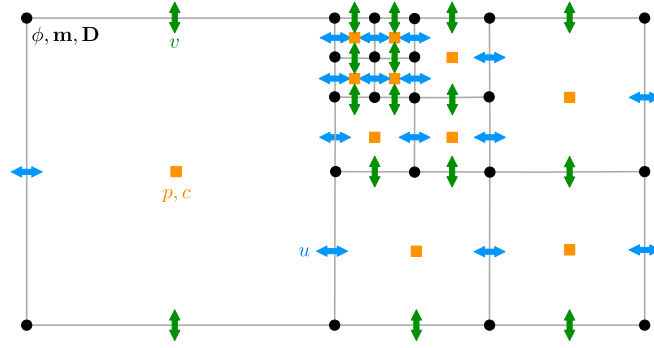
Fig. 2. Data layout: Velocity components (u, v) are stored at the faces of the cells, whereas pressure p and concentration c are stored at the cell centers. All the other quantities, such as the polarization $\mathbf{m}$, nematic tensor $\mathbf{D}$ and level set ϕ are stored at the nodes of the mesh.

where $\mathrm{Lip}(\phi)$ is the Lipschitz constant of the level set function ϕ, $\mathrm{diag}(C)$ is the length of the diagonal of cell C, and $\max_{\mathrm{level}}$ is the predefined maximum level of the tree. By replacing $\mathrm{Lip}(\phi)$ by the appropriate quantity, the above criterion can easily be adapted to enforce the resolution inside a uniform band of arbitrary width surrounding the interface.

Second, to systematically adapt the mesh to the spatial variations of the solution variables $(c, \mathbf{m}, \mathbf{D}, \mathbf{u})$, we recursively split any cell C in which the relative variation in the solution exceeds a fixed threshold T_V:

$$\max_{v \in \mathrm{nodes}(C)} \max \left(\frac{||\nabla c(v)||_\infty}{||c||_\infty}, \frac{||\nabla \mathbf{m}(v)||_\infty}{||\mathbf{m}||_\infty}, \frac{||\nabla \mathbf{D}(v)||_\infty}{||\mathbf{D}||_\infty}, \frac{||\nabla \mathbf{u}(v)||_\infty}{||\mathbf{u}||_\infty} \right) \geq T_V \quad \text{and} \quad \mathrm{level}(C) < \max_V, \tag{66}$$

where $|| \cdot ||_\infty$ is the L^∞-norm and $\max_V$ is the maximum level of refinement for the gradient-based refinement.

5.2. Data structure

Fig. 2 illustrates how the data is laid out. Fluid flow variables $(\mathbf{u}, p)$ are stored using the standard Marker And Cell (MAC) scheme, with the pressure stored at cell centers and velocity components on cell faces. The concentration field c is also stored at the cell centers to allow for conservative discretizations of the diffusive and coupling terms in the Poisson problem (54) (see section 6.1). The choice of a conservative scheme for c is motivated by the desire to conserve the total mass of swimmers in the system; note, however, that the discretization of advective terms using the SLBDF method is non-conservative. The polarization $\mathbf{m}$ and nematic tensor $\mathbf{D}$ are both stored at the nodes of the Quadtree for increased accuracy (see section 6.2). Finally, following previous work [36,56–58,38,19], we also store values of the level set function ϕ at the nodes.

For computational efficiency, we also store copies of the velocity and concentration field at the nodes. These copies are created as third-order accurate interpolations of the original quantities. They are used to reconstruct the semi-Lagrangian trajectories, interpolate the concentration at the departing points and calculate nonlinear coupling terms involving the concentration. Additionally, a copy of the polarization components interpolated at the faces is also stored. As we explain in the next section, this copy is used for discretization of the concentration equation (54).

6. Spatial discretizations

6.1. Finite volume method for the concentration

The Poisson problem (54) along with the Neumann boundary condition (55) is discretized using a second-order finite-volume method. To each cell center i, we associate the control volume V_i defined as the intersection of the cell C_i with the interior of the domain Ω:

$$V_i = C_i \cap \Omega. \tag{67}$$

Integrating Eq. (54) over V_i and using the divergence theorem yields

$$\beta \int_{V_i} c_{k+1}^{n+1} + \Lambda Pe_s^2 \int_{\partial V_i} \mathbf{n} \cdot \nabla c_{k+1}^{n+1} = -\int_{V_i} \left(\gamma c_d^n - \delta c_d^{n-1} \right) + Pe_s \int_{V_i} \nabla \cdot \mathbf{m}_k^{n+1}. \tag{68}$$

Approximating volume integrals by the value of the integrand at the center of V_i, we obtain:

$$\beta V_i c_{k+1}^{n+1}(i) + \Lambda Pe_s^2 \int_{\partial V_i} \mathbf{n} \cdot \nabla c_{k+1}^{n+1} = -V_i \left[\gamma c_d^n(i) - \delta c_d^{n-1}(i) \right] + Pe_s \int_{V_i} \nabla \cdot \mathbf{m}_k^{n+1} + \mathcal{O}(\Delta x^3). \tag{69}$$
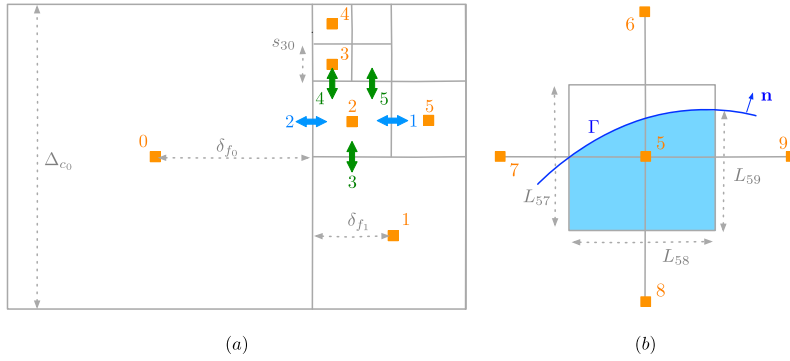
Fig. 3. Cell-based finite volume method for the concentration field: general configuration away from (a) and close to (b) the interface.

In order to further discretize the remaining integrals, we distinguish mesh cells that are away from the domain boundaries from those that intersect it.

6.1.1. Away from domain boundaries

Far away from walls, the control volume V_i is simply the grid cell C_i, the contour ∂C_i is the contour of the cell and therefore discretizing Eq. (69) requires approximating the fluxes $\mathbf{n} \cdot \nabla c_{k+1}^{n+1}$ on each of the faces of the cell. For example, referring to Fig. 3(a), the discretization at cell 2 requires calculation of the fluxes at faces 1, 2, 3, 4 and 5. In general, for any such cell C_i, the normal gradient of concentration $\mathbf{n} \cdot \nabla c_{k+1}^{n+1}\big|_f$ across face f is approximated with second-order accuracy following the method presented in [30] and using the formulation of [19] as

$$\mathbf{n} \cdot \nabla c_{k+1}^{n+1}\big|_f = \sum_{\substack{j \in C(f) \\ j \neq i}} \frac{s_{ij}}{\Delta_{c_i}} \left(\frac{c_{k+1}^{n+1}(i) - c_{k+1}^{n+1}(j)}{\Delta_f} \right) + \mathcal{O}(\Delta x^2), \tag{70}$$

where $C(f)$ is the set of indices of cells connected to face f (i.e., the cell neighbors of face f). If the face f separates two cells of equal size, then this set only contains these two cells. For instance, in Fig. 3(a) we have $C(1) = \{2, 5\}$. If f separates two cells of different sizes, we denote by C_L the larger cell and define $C(f)$ as the list of cell neighbors of C_L across its side containing f, including C_L itself. As an example, face 2 in Fig. 3(a) separates cells 0 and 2, where the large cell is 0 with face 2 on its right side. Therefore $C(2)$ is the set of right cell neighbors of cell 0, including 0 itself: $C(2) = \{0, 1, 2, 3, 4\}$.

The coefficient s_{ij} is the length of the segment separating cells i and j, Δ_{c_i} is the linear size of cell i, and the average distance Δ_f is defined as:

$$\Delta_f = \sum_{\substack{j \in C(f) \\ j \neq i}} \frac{s_{ij}}{\Delta_{c_i}} \left(\delta_{fi} - \delta_{fj} \right), \tag{71}$$

where δ_{fi} is the signed distance from cell i to face f.

The last term in Eq. (69) is approximated using the copy of the polarization at the cell faces and the formula for the discrete divergence presented in [19]. Specifically, for cell i,

$$\nabla \cdot \mathbf{m}_k^{n+1}\big|_i = -\frac{1}{\Delta_{c_i}} \sum_{j \in F(i)} \frac{s_j \tilde{m}_k^{n+1}(j)}{A_j} \frac{\delta_{ji}}{|\delta_{ji}|} + \mathcal{O}(\Delta x^2) \quad \text{where} \quad A_f = \frac{1}{2} \sum_{j \in C(f)} s_j, \tag{72}$$

where $F(i)$ is the set of faces in contact with cell i, and $\tilde{m}_k^{n+1}(j)$ is the normal component of the polarization at face j.

6.1.2. Close to the interface

The finite volume equation (69) applied to a cell i that intersects the boundary ($C_i \cap \Omega \neq \emptyset$) simplifies to

$$\beta V_i c_{k+1}^{n+1}(i) + Pe_s \int_{\partial V_i - \partial \Omega} \mathbf{n} \cdot \left(\Lambda Pe_s \nabla c_{k+1}^{n+1} + \mathbf{m}_k^{n+1} \right) = -V_i \left[\gamma c_d^n(i) - \delta c_d^{n-1}(i) \right] + \mathcal{O}(\Delta x^3), \tag{73}$$

where we have used the boundary condition (55) to cancel out the flux across $\partial \Omega$, and where the area V_i of the control volume is approximated with second-order accuracy using the technique described in [35]. The only term that remains to be discretized is the contour integral over $\partial V_i - \partial \Omega$. This is achieved using the approximation
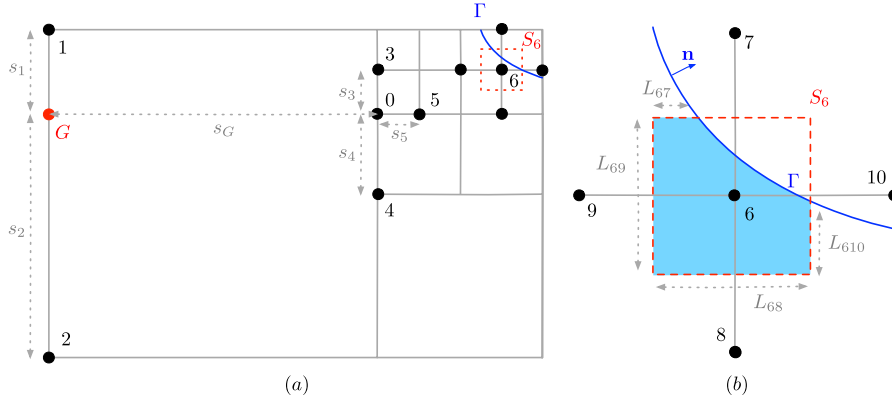
Fig. 4. Hybrid finite difference/volume method on a Quadtree. (a) Away from the interface, finite differences can be used systematically by defining ghost nodes and values when T-junctions occur. (b) The finite volume method is used close to the interface, where Neumann boundary conditions need to be enforced.

$$\int_{\partial V_i - \partial \Omega} \mathbf{n} \cdot \left(\Lambda P e_s \nabla c_{k+1}^{n+1} + \mathbf{m}_k^{n+1} \right) = \sum_{j \in N(i)} L_{ij} \left(\Lambda P e_s \frac{c_{k+1}^{n+1}(j) - c_{k+1}^{n+1}(i)}{\Delta x} + \tilde{m}_k^{n+1}(i,j) \right) + \mathcal{O}(\Delta x^3), \tag{74}$$

where $N(i)$ is the set of the direct cell neighbors of cell i, L_{ij} is the fraction of the face separating cells i and j that is contained in the domain Ω (see Fig. 3), and $\tilde{m}_k^{n+1}(i,j)$ is the interpolation of the normal component of the polarization at the center of the face separating cells i and j. We note that if one of the direct cell neighbors k of cell i is not at least partially inside the domain Ω (for example, cell 6 in Fig. 3), then the length fraction L_{ik} is zero and cell k does not contribute to Eq. (74) as expected.

6.1.3. Remarks

The linear system resulting from the combination of these two discretization strategies is symmetric positive definite. Furthermore, it can be shown using formulas (70), (72) and (74) that the discretization of the diffusive and coupling effects is conservative, i.e., it preserves the total mass in the system. Our discretization of the advective terms (SLBDF), however, does not share this property and can therefore introduce variations in the total mass. Based on the accuracy of the above discretizations, we expect the determination of c_{k+1}^{n+1} to be second-order accurate.

Once the new concentration field has been computed in Ω as a solution of the discretized system, it is extended to the entire domain using a geometric extension procedure [19]. From this extension, the nodal copy is constructed using a third-order-accurate least-squares interpolation.

6.2. Higher moments: hybrid finite difference/finite volume method

Equations (56) and (58) for the polarization and nematic tensor fields are discretized in space using the second-order hybrid finite difference/finite volume method we developed in [56]. Because $\mathbf{m}_{k+1}^{n+1}$ and $\mathbf{D}_{k+1}^{n+1}$ are tensors of order 1 and 2, respectively, this procedure must be applied to all their components: m_x, m_y, D_{xx}, D_{xy}, D_{yx} and D_{yy} in two dimensions.

6.2.1. Finite differences on a Quadtree

The right-hand sides in Eqs. (56), (58) and boundary conditions (57), (59) are discretized using the Finite Difference on Quadtree method of Min et al. [37,36]. To illustrate how these discretizations are constructed we consider the general configuration shown in Fig. 4. Assume that we are interested in discretizing a node-based quantity ψ at node 0, which has three direct neighbors $\{3, 4, 5\}$ but none in the left direction. To compensate for this missing neighbor, a ghost node G is introduced, where we approximate the quantity ψ with third-order accuracy using existing neighboring nodes:

$$\psi_G = \frac{\psi_2 s_1 + \psi_1 s_2}{s_1 + s_2} - \frac{s_1 s_2}{s_3 + s_4} \left(\frac{\psi_3 - \psi_0}{s_3} + \frac{\psi_4 - \psi_0}{s_4} \right) + \mathcal{O}\left(\Delta x^3 \right), \tag{75}$$

where Δx is the maximum spatial resolution. Using the above ghost value along with classical second-order finite-difference formulas, the standard differential operators can be discretized. For example the discrete first and second derivatives in the x-direction at node 0 are expressed as

$$\mathcal{D}_x^0(\psi) = \frac{\psi_5 - \psi_0}{s_5} \frac{s_G}{s_5 + s_G} + \frac{\psi_0 - \psi_G}{s_G} \frac{s_5}{s_5 + s_G}, \tag{76}$$

$$\mathcal{D}_{xx}^0(\psi) = \frac{2}{s_5 + s_G} \left(\frac{\psi_5 - \psi_0}{s_5} + \frac{\psi_G - \psi_0}{s_G} \right), \tag{77}$$

and similarly in the y-direction

$$\mathcal{D}_y^0(\psi) = \frac{\psi_3 - \psi_0}{s_3} \frac{s_3}{s_3 + s_4} + \frac{\psi_0 - \psi_4}{s_4} \frac{s_4}{s_3 + s_4}, \tag{78}$$

$$\mathcal{D}_{yy}^0(\psi) = \frac{2}{s_3 + s_4} \left(\frac{\psi_3 - \psi_0}{s_3} + \frac{\psi_4 - \psi_0}{s_4} \right). \tag{79}$$

A standard Taylor series analysis shows that the above formulas for the first derivatives $\mathcal{D}_x^0$, $\mathcal{D}_y^0$ are second-order accurate, while those for $\mathcal{D}_{xx}^0$, $\mathcal{D}_{yy}^0$ are at least first-order accurate. In practice, both are found to be second-order accurate, and we refer the interested reader to [37,36,38,39] for convergence results.

Using the above discretization formulas and third-order extensions of the nodal values, the right-hand sides of Eq. (56), (58) and boundary conditions (57), (59) can be discretized at every node of the mesh with second-order accuracy, yielding

$$\left(-\gamma \mathbf{m}_d^n - \delta \mathbf{m}_d^{n-1} - Pe_s \nabla \cdot \left(\mathbf{D}_k^{n+1} + c_{k+1}^{n+1} \frac{\mathbf{I}}{2} \right) + \mathbf{H}_{m,k}^{n+1} \right) \Big|_i = \mathcal{R}_m(i) + \mathcal{O}(\Delta x^2), \tag{80}$$

$$\left(-\gamma \mathbf{D}_d^n - \delta \mathbf{D}_d^{n-1} - Pe_s \nabla \cdot \left(\mathbf{T}_{k+1}^{n+1} - \mathbf{m}_{k+1}^{n+1} \frac{\mathbf{I}}{2} \right) + \mathbf{H}_{D,k}^{n+1} \right) \Big|_i = \mathcal{R}_D(i) + \mathcal{O}(\Delta x^2),$$

and

$$\Lambda Pe_s^2 \mathbf{n} \cdot \nabla \mathbf{m}_{k+1}^{n+1} = \mathcal{G}_m(i) + \mathcal{O}(\Delta x^2), \tag{81}$$

$$\Lambda Pe_s^2 \mathbf{n} \cdot \nabla \mathbf{D}_{k+1}^{n+1} = \mathcal{G}_D(i) + \mathcal{O}(\Delta x^2).$$

At nodes away from the interface, the diffusive terms in the left-hand sides of (56), (58) are also approximated using the same finite difference technique.

6.2.2. Finite volumes

Close to the interface, where the mesh is uniform and the Neumann boundary conditions (57), (59) need to be enforced, Eqs. (56), (58) are discretized using a finite volume method. Since both equations have the same form, we only show details for the polarization. To any node i close to the interface we associate a control volume V_i defined as the intersection of the square S_i centered at i and of size Δx with Ω (see Fig. 4). Integrating Eq. (56) over V_i and applying Gauss's theorem yields

$$\int_{V_i} (1+\beta)\mathbf{m}_{k+1}^{n+1} + \int_{\partial V_i} \Lambda Pe_s^2 \mathbf{n} \cdot \nabla \mathbf{m}_{k+1}^{n+1} = \int_{V_i} \left(-\gamma \mathbf{m}_d^n - \delta \mathbf{m}_d^{n-1} - Pe_s \nabla \cdot \left(\mathbf{D}_k^{n+1} + c_{k+1}^{n+1} \frac{\mathbf{I}}{2} \right) + \mathbf{H}_{m,k}^{n+1} \right). \tag{82}$$

The integral on the right-hand side is approximated with second-order accuracy using the finite difference approximation (80) and the volume integral techniques discussed in [35]. The volume integral on the left-hand side is approximated using V_i and the node value as

$$\int_{V_i} (1+\beta)\mathbf{m}_{k+1}^{n+1} = V_i(1+\beta)\mathbf{m}_{k+1}^{n+1}(i) + \mathcal{O}(\Delta x^4). \tag{83}$$

The remaining contour integral over ∂V_i is first decomposed into two parts

$$\int_{\partial V_i} \Lambda Pe_s^2 \mathbf{n} \cdot \nabla \mathbf{m}_{k+1}^{n+1} = \int_{\partial V_i - \partial\Omega} \Lambda Pe_s^2 \mathbf{n} \cdot \nabla \mathbf{m}_{k+1}^{n+1} + \int_{\partial\Omega} \Lambda Pe_s^2 \mathbf{n} \cdot \nabla \mathbf{m}_{k+1}^{n+1}. \tag{84}$$

The first integral over $\partial V_i - \partial\Omega$ is treated exactly like the contour integral for the concentration in section 6.1: if $N(i)$ are the direct neighbors of node i and L_{ij} is the fraction of the sides of S_i separating nodes i and j (see Fig. 4), then

$$\int_{\partial V_i - \partial\Omega} \Lambda Pe_s^2 \mathbf{n} \cdot \nabla \mathbf{m}_{k+1}^{n+1} = \sum_{j \in N(i)} L_{ij} \frac{\mathbf{m}_{k+1}^{n+1}(j) - \mathbf{m}_{k+1}^{n+1}(i)}{\Delta x} + \mathcal{O}(\Delta x^3). \tag{85}$$

The second integral over $\partial\Omega$ is calculated using the finite difference approximation (81) and the contour integral procedure described in [35].

6.2.3. Remarks

As for the concentration, we expect both the polarization and nematic order to be second-order accurate in L^∞-norm, based on our approximations and on the accuracy of the computational techniques (extensions, volume and contour integrations, interpolations). Unlike for the concentration, whose discretization results in a linear system that is symmetric positive definite, the discretized systems for the higher moments are only positive definite. The symmetry is lost when using the finite difference method to discretize the diffusive terms. In practice, the linear systems are solved using a Bi-Conjugate Gradient Stabilized method with a Multigrid solver [58] acting as a preconditioner. As for the concentration, all moment components are extended to the entire domain with a third-order extension procedure [3,36] so that interpolations and numerical derivatives can be accurately computed close to the interface.

6.3. Projection of the nematic tensor

The nematic tensor $\mathbf{D}$ as defined in Eq. (9) is trace-free and symmetric. In theory, we could get away with solving for only two components of $\mathbf{D}$ (one diagonal and one off-diagonal) and reconstruct the other two. In practice, we cannot decide *a priori* which diagonal/off-diagonal components to solve for as they may differ by numerical errors. We therefore solve for all four components of $\mathbf{D}_{k+1}^{n+1}$ and project the result on the space of trace-free symmetric tensors. Omitting the sub/superscripts, the projected tensor $\mathcal{P}(\mathbf{D})$ is obtained as

$$\mathcal{P}(\mathbf{D}) = \mathbf{D} - \frac{\text{Tr}(\mathbf{D})}{2}\mathbf{I} - \frac{\mathbf{D} - \mathbf{D}^T}{2}, \tag{86}$$

where $\text{Tr}(\mathbf{D})$ is the trace of $\mathbf{D}$, and $\mathbf{D}^T$ is its transpose. This projection is stable in any tensor norm $\|\cdot\|$, i.e.,

$$\|\mathcal{P}(\mathbf{D})\| \leq \|\mathbf{D}\|, \tag{87}$$

and therefore it does not affect the stability of the overall method.

Proof. As all norms are equivalent in finite dimension, we choose to use the Frobenius norm $\|\mathbf{D}\|^2 = \mathbf{D} : \mathbf{D}$. To prove the stability of the projection, it is sufficient to prove that it is orthogonal, i.e.,

$$\mathcal{P}(\mathbf{D}) : (\mathcal{P}(\mathbf{D}) - \mathbf{D}) = 0, \tag{88}$$

since it implies that

$$\|\mathbf{D}\|^2 = \|\mathcal{P}(\mathbf{D}) - (\mathcal{P}(\mathbf{D}) - \mathbf{D})\|^2 = \|\mathcal{P}(\mathbf{D})\|^2 + \|\mathcal{P}(\mathbf{D}) - \mathbf{D}\|^2 \geq \|\mathcal{P}(\mathbf{D})\|^2. \tag{89}$$

Expanding Eq. (88), we obtain

$$\mathcal{P}(\mathbf{D}) : (\mathcal{P}(\mathbf{D}) - \mathbf{D}) = \frac{1}{2}\text{Tr}(\mathcal{P}(\mathbf{D}))\,\text{Tr}(\mathbf{D}) - \mathcal{P}(\mathbf{D}) : \frac{\mathbf{D} - \mathbf{D}^T}{2}. \tag{90}$$

Since $\mathcal{P}(\mathbf{D})$ is trace-free by construction, the first term vanishes and, after a second expansion, we are left with

$$\mathcal{P}(\mathbf{D}) : (\mathcal{P}(\mathbf{D}) - \mathbf{D}) = -\frac{1}{2}\left(\|\mathbf{D}\|^2 - \mathbf{D} : \mathbf{D}^T - \frac{1}{2}\text{Tr}(\mathbf{D})\text{Tr}(\mathbf{D} - \mathbf{D}^T) - \frac{1}{2}\|\mathbf{D} - \mathbf{D}^T\|^2\right), \tag{91}$$

$$= -\frac{1}{4}\left(-\text{Tr}(\mathbf{D})\text{Tr}(\mathbf{D} - \mathbf{D}^T) + \|\mathbf{D}\|^2 - \|\mathbf{D}^T\|^2\right). \tag{92}$$

Because $\mathbf{D} - \mathbf{D}^T$ has zeros on its diagonal and $\|\mathbf{D}^T\| = \|\mathbf{D}\|$, the right-hand side vanishes and Eq. (88) is satisfied. □

6.4. Fluid flow

At each time step, we differentiate the newly obtained nematic order tensor $\mathbf{D}_{k+1}^{n+1}$ using the finite difference method described in section 6.2.1 to compute the active force density $\alpha\nabla\cdot\mathbf{D}_{k+1}^{n+1}$. The momentum and continuity equations (40) and (41) for the motion of the fluid are then solved using the incompressible Navier-Stokes solver previously developed by Guittet, Theillard & Gibou in [19], where the active force density enters as a standard body force.

While we omit details of the method for brevity and refer the interested to the original article [19], we would like to comment on its stability and accuracy. First, the Navier-Stokes solver was shown to be unconditionally stable and therefore does not compromise the stability of the overall algorithm or add any time step restriction. Second, we note that the velocity field produced by the solver is less than second-order accurate, but has at least first-order accuracy. In light of our previous remarks, we therefore expect the velocity field to be the least accurate quantity and to limit the accuracy on the other parts of the solution.

6.5. Time step

Since both the time discretization and the fluid solver are stable, the choice of time step is motivated primarily by the convergence of functional iterations, the desired accuracy of the solution and constraints on computational time. Specifically, we define the time step based on the current fluid velocity $\mathbf{u}$ and apparent mean swimming velocity $\mathbf{v} = Pe_s\mathbf{m}/c$ as

$$\Delta t_n = \max\left(\frac{1}{\|\mathbf{u}\|_\infty}, \frac{1}{\|\mathbf{v}\|_\infty}, 1\right)\Delta x, \tag{93}$$

where Δx is the minimum grid size. Using this definition, we find that functional iterations converge exponentially fast, and the numerical solution was obtained rapidly with a good accuracy.

7. Numerical examples

We illustrate the capabilities of our method on a number of examples in both two and three dimensions. The examples are motivated by previous experiments on suspensions of swimming bacteria, and consequently we take $\zeta = 1$, which corresponds to slender swimmers. We also assume that inertial effects are negligible (as is typically the case in bacterial suspensions and other active fluids) and therefore set the Reynolds number to $Re = 10^{-6}$.

7.1. Code validation

7.1.1. Steady-state analytical solution for the first two moments
Analytical solutions of the non-linear coupled system of Eqs. (10), (11), (12) and (20), (21) for arbitrary parameters and geometries are unavailable in general. The system can, however, be simplified in certain geometries after introducing additional assumptions. We consider here the case of a two-dimensional circular domain of radius a, where we assume axisymmetry for the solution and neglect the nematic tensor ($\mathbf{D} = \mathbf{0}$). This approximation, while seemingly crude, has been shown in the past to yield solutions that are close to the full system [55]. Under these assumptions, there is no fluid flow in the system, and the steady concentration and radial polarization profiles can be obtained analytically as

$$c_{\text{exact}}(r) = c_0 + c_1\mathcal{I}_0(\rho r), \tag{94}$$

$$m_{r,\text{exact}}(r) = c_1\Lambda Pe_s\rho\mathcal{I}_1(\rho r), \tag{95}$$

where $\mathcal{I}_\nu(x)$ is the modified Bessel function of the first kind of order ν, and the constants ρ, c_0, c_1 are given by

$$\rho = \frac{\sqrt{\Lambda Pe_s - 1}}{\Lambda Pe_s}, \tag{96}$$

$$c_0 = \left(1 + \frac{2\mathcal{I}_1(\rho a)}{a\rho\big[\Lambda^2 Pe_s^2\rho^2\left(\mathcal{I}_0(\rho a) + \mathcal{I}_2(\rho a)\right) - \mathcal{I}_0(\rho a)\big]}\right)^{-1}, \tag{97}$$

$$c_1 = \frac{c_0}{\Lambda^2 Pe_s^2\rho^2\left(\mathcal{I}_0(\rho a) + \mathcal{I}_2(\rho a)\right) - \mathcal{I}_0(\rho a)}. \tag{98}$$

We validate our numerical approach by comparing the above solution to a numerical solution obtained by neglecting $\mathbf{D}$. We choose the parameters and initial conditions as follows:

$$Pe_s = 1, \quad \Lambda = 1, \quad a = 0.5, \quad c(r, 0) = 1, \quad \mathbf{m}(r, 0) = \mathbf{0}, \quad t_f = 50, \quad \Delta t = 20\Delta x, \quad \Omega = [-1, 1]^2, \tag{99}$$

where t_f is the final time and Δx the minimum grid resolution. The numerical solution is run to steady state and compared to Eqs. (94)–(95). To estimate the order of convergence of our method, we first run the simulation on a grid with $\max_{\text{level}} = 5$ and $\min_{\text{level}} = 2$, and then recursively repeat the same calculation on finer grids, each time increasing $\min_{\text{level}}$ and $\max_{\text{level}}$ by one. The mesh is only refined in the vicinity of the boundary, where the gradients in the solution are located. By this method, the spatial resolution is almost systematically divided by a factor of 2 everywhere in the domain from one simulation to the next, and the ratio of the error on these two grids thus provides an estimate for the convergence order. The L^∞-errors for both moments as functions of time are depicted in Fig. 5, and the estimated orders of convergence are given in Table 1. We observe second-order convergence for both quantities, which is consistent with our theoretical predictions in sections 6.1 and 6.2. In addition to converging with the expected order, both errors are reasonably small even on the coarsest grids. Their values provide rough estimates of expected errors on the moments in other cases with similar parameters when the fluid flow and nematic order tensor are no longer neglected and should help select the tree resolution in these situations.

This example does not validate our time discretization (SLBDF method) nor the discretization of the nematic tensor. Nevertheless, the equations for the nematic tensor and polarization are discretized using the same approach so we expect
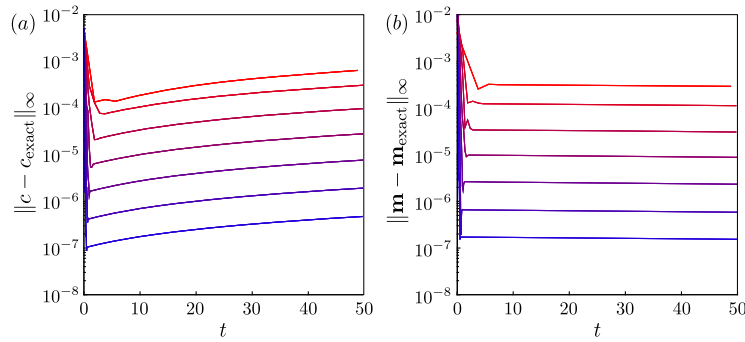
Fig. 5. Comparison with the analytical solution of Eqs. (94) and (95): L^∞-error of the concentration (a) and polarization (b) as functions of time. The red curves are associated to the coarsest levels, the blue ones with the finest ones.

Table 1
Final errors and corresponding estimates for the orders of convergence of the concentration and polarization, in the case of the analytical example of section 7.1.1.

Quadtree level	Concentration		Polarization	
(min / max)	L^∞ error	Order	L^∞ error	Order
2 / 5	6.381×10^{-4}	–	2.914×10^{-4}	–
3 / 6	3.071×10^{-4}	1.055	1.122×10^{-4}	1.379
4 / 7	9.701×10^{-5}	1.661	3.060×10^{-5}	1.874
5 / 8	2.803×10^{-5}	1.791	8.778×10^{-6}	1.801
6 / 9	7.675×10^{-6}	1.869	2.330×10^{-6}	1.913
7 / 10	1.928×10^{-6}	1.993	5.845×10^{-7}	1.995
8 / 11	4.767×10^{-7}	2.016	1.453×10^{-7}	2.008

both quantities to converge at similar rates. Additionally, we refer the interested reader to [7,19,36] for a detailed analysis of the SLBDF method used here. Overall, we are confident that our method is correctly implemented and that it accurately captures the evolution of these three moments in the absence of flow.

7.1.2. Parasitic flows in suspensions of pullers

As a further test of our method, we analyze the dynamics in a suspension of so-called puller particles for which $\alpha > 0$. In this system, active stresses are known to have a stabilizing effect and to damp any fluid flow, leading to a quiescent steady state. This provides a simple benchmark for our code, as the magnitude of any parasitic fluid flow that persists in the system at steady state quantifies numerical errors. We perform two-dimensional simulations in a circular disk of radius a with parameters

$$Pe_s = 1, \quad \Lambda = 1, \quad \alpha = 50, \quad a = 0.5, \quad t_f = 10, \quad \Delta t = 20\Delta x, \quad \Omega = [-1, 1]^2. \tag{100}$$

The mesh is automatically refined using the refinement criteria discussed in section 5.1, with the following parameters:

$$T_V = 0.02, \qquad \max_V = \max_{\text{level}} - 1, \qquad \min_{\text{level}} = 3, \tag{101}$$

and multiple identical simulations are performed on grids with increasing values of $\max_{\text{level}}$. The convergence of the method is validated by monitoring mass losses as well as the norm of the parasitic fluid velocity as functions of time. Fig. 6 shows both quantities, and the corresponding estimates for the order of accuracy are given in Table 2. The convergence of the parasitic flows is consistent with the accuracy of the flow solver as discussed previously, with an order between 1 and 2. Since the moments are now coupled to the flow through the gradient of the velocity field, their accuracy is limited by that of the velocity gradient, which is less accurate than the velocity. This explains the slower convergence reported in Table 2 for the total mass.

7.2. Instabilities and spontaneous flows in pusher suspensions in circular domains

We now turn our attention to the active fluid flow generated by a suspension of pushers ($\alpha < 0$) in a circular domain of radius a. This case is representative of suspensions of bacteria and is known to exhibit transitions to spontaneous flows as a result of hydrodynamic instabilities driven by active stresses [48,49,46,15,55]. We use the following physical and numerical parameters:

$$Pe_s = 0.5, \quad \Lambda = 0.1, \quad a = 0.5, \quad t_f = 5, \quad \Omega = [-1, 1]^2, \tag{102}$$

and we systematically vary the magnitude α of the active stress tensor.
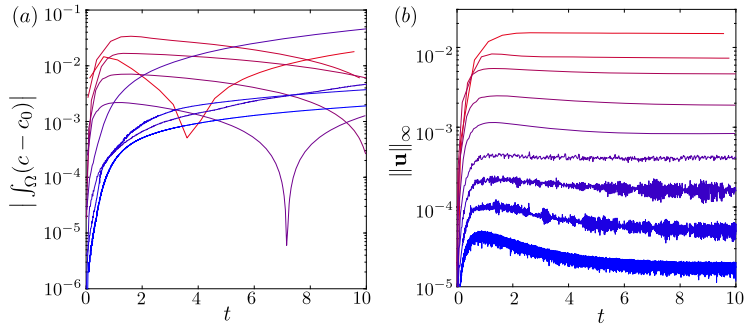
Fig. 6. Suspension of pullers: total concentration variation (a) and magnitude of the parasitic flow (b) as functions of time. The red curves are associated to the coarsest levels, the blue ones with the finest ones.

Table 2
Final errors and corresponding estimates for the orders of convergence of the total mass and norm of the parasitic flow in the example of section 7.1.2.

| $\max_{level}$	Total mass		Velocity	
	Error	Order	L^∞ error	Order
3	1.796×10^{-2}	–	1.491×10^{-2}	–
4	3.388×10^{-2}	-0.915	7.340×10^{-3}	1.023
5	1.672×10^{-2}	1.018	4.663×10^{-3}	0.654
6	7.093×10^{-3}	1.237	1.890×10^{-3}	1.302
7	2.191×10^{-3}	1.695	8.340×10^{-4}	1.181
8	8.429×10^{-2}	-5.265	3.907×10^{-4}	1.094
9	4.707×10^{-3}	4.162	1.616×10^{-4}	1.274
10	3.736×10^{-3}	0.333	5.255×10^{-5}	1.621
11	1.910×10^{-3}	0.967	1.590×10^{-5}	1.724
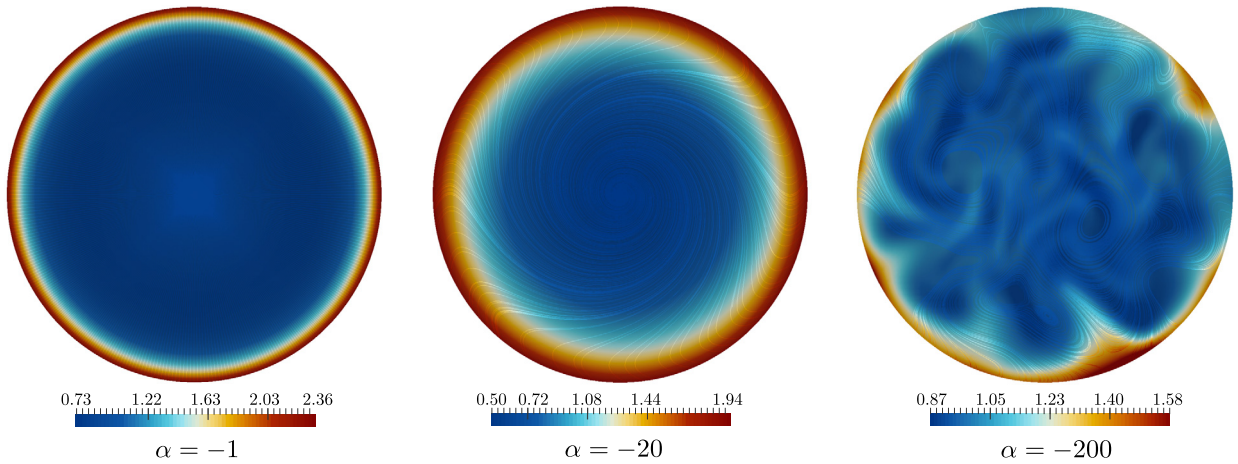
Fig. 7. Typical flow patterns in an active suspension confined inside a circular disk. Simulations are performed on a grid with $\max_{level} = 8$, for $\Lambda = 0.1$, $Pe_s = 0.5$ and increasing activity levels. Both the streamlines of the net velocity and the concentration field are shown.

We previously analyzed this problem in our recent work [55], where we considered a variety of elementary geometries and also characterized the transitions between regimes using stability analyses; we only briefly summarize the results here, and the reader is referred to [55] for a more detailed analysis and discussion of the dynamics as well as comparison with experiments. Our study identified three typical states, which Fig. 7 illustrates. The transitions between these three states can be observed by increasing the activity level $|\alpha|$ while maintaining all other parameters constant. At low levels of activity (Fig. 7, $\alpha = -1$), the swimmers accumulate at the boundary and have a net average polarization towards the wall. This wall accumulation is a hallmark of suspensions of self-propelled particles and has been characterized in both experiments [43,28,27] and models [26,10,11,14]. There is no fluid flow in this regime, and the solution is similar to the analytical solution discussed in 7.1.1 (e.g., radial symmetry, wall accumulation and wall-normal polarization, weak nematic alignment). At intermediate levels of activity ($\alpha = -20$), a spontaneous steady azimuthal fluid flow emerges causing the swimmers to reorient against the flow. The resulting apparent velocity exhibits a double vortex structure similar to that observed
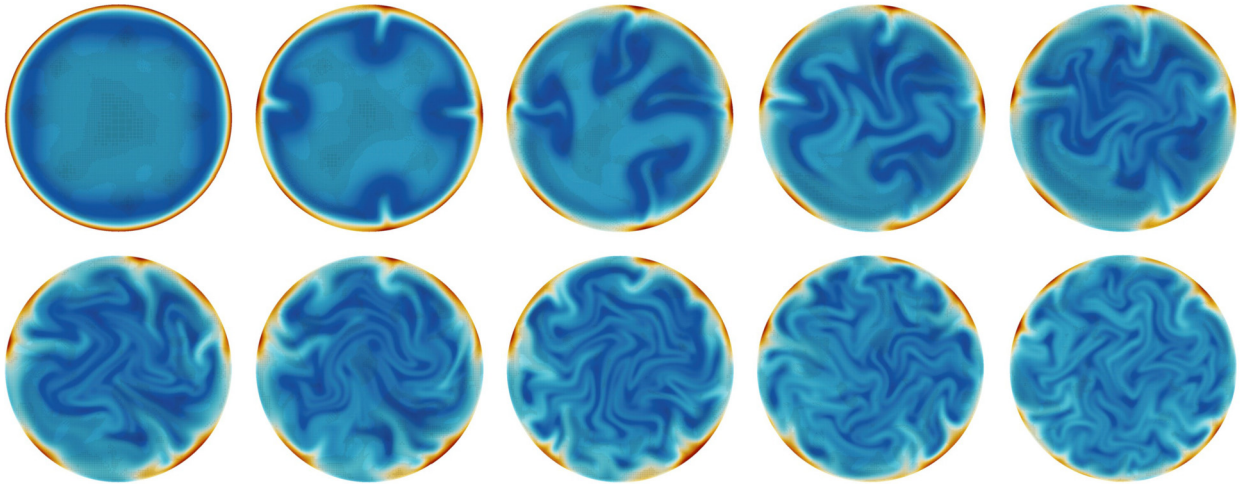
Fig. 8. Suspensions of pushers inside a disk: spontaneous flow destabilization at high activity level ($\Lambda = 0.1$, $Pe_s = 0.5$ and $\alpha = -200$), for times between 0 and 1. The adaptive mesh is also shown to illustrate how it is dynamically adapted to the solution.
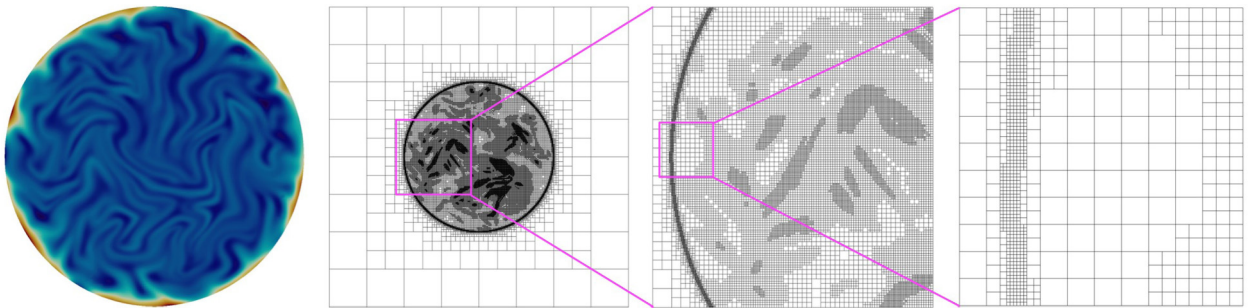
Fig. 9. Adaptive mesh refinement for a suspension of pushers inside a disk in the unstable regime: (left) concentration profile, and (right) successive zoom on the adaptive mesh at time $t_f = 0.6$. Parameter values: $\Lambda = 0.1$, $Pe_s = 0.3$ and $\alpha = -300$.

experimentally by Wioland et al. [63,32]. This transition was explained in our previous work [55] as the result of a linear instability of the quiescent state, which is driven by active stresses. In very active systems ($\alpha = -200$), the double-vortex is no longer stable and the system transitions to a chaotic regime characterized by unsteady swirls and vortices similar to those observed in bulk systems [15]. Fig. 8 illustrates the destabilization process in this regime.

Fig. 9 illustrates the automatic mesh refinement to the solution for a suspension of pushers in the unsteady chaotic regime ($Pe_s = 0.3$, $\Lambda = 0.1$, $\alpha = -300$) using a high resolution grid ($\max_{level} = 11$, $T_V = T_M = 0.05$, $\max_V = \max_C = 10$, $\min_{level} = 3$) at a final time of $t_f = 0.6$. The total number of nodes is 87 532 which is only 2.09% of the size of a uniform mesh with the same maximum resolution. Because the refinement criterion (66) depends continuously on the solution, we find that the mesh is almost graded. Yet non-gradedness does arise in some regions, typically close to the interface.

7.3. Active fluid flows in periodic lattices

Inspired by the microfluidic experiments of Wioland et al. [62], we now apply our simulation method to study active flows in periodic lattices. The geometry of the lattice is described in Fig. 10, and is composed of circular chambers connected by junctions. We select parameters such that a steady double vortex would spontaneously emerge in the unit cell when the junctions are closed and study how the direction of rotation between adjacent cells and the overall system dynamics depend on the width of the gap ($2a$) connecting them. Specifically, we use the parameters

$$Pe_s = 2, \quad \Lambda = 0.1, \quad \alpha = -100, \quad t_f = 5, \quad \Omega = [0, 20]^2, \tag{103}$$

and the mesh is constructed using

$$\max_{level} = 11, \qquad T_V = T_M = 0.02, \qquad \max_V = \max_C = 10, \qquad \min_{level} = 3. \tag{104}$$
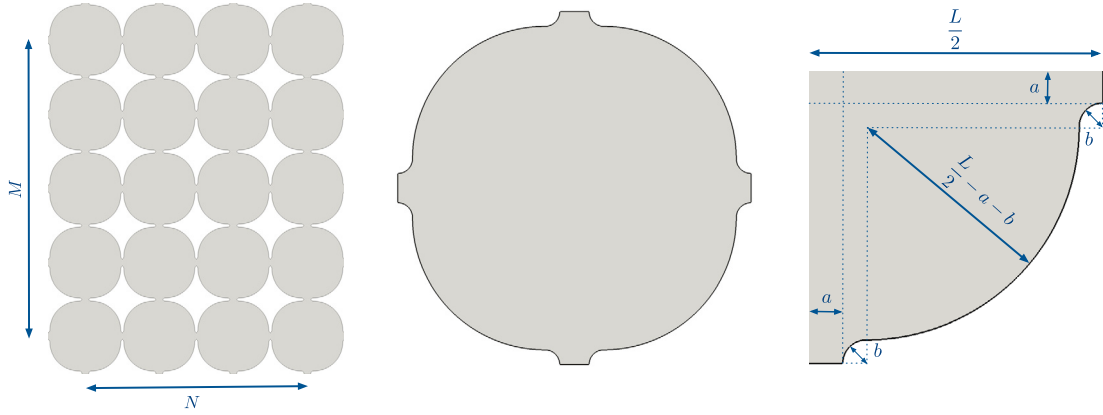
Fig. 10. Active flows in lattices: geometric parametrization. For the simulations presented here we use a lattice with 17×13 individual cells. We take the diameter of the unit cell to be $L = 1$ and set $b = 0.0278$.

Following [62], we define the time-averaged normalized spin-spin correlation as

$$\chi = \frac{1}{t_f} \int_0^{t_f} \frac{\sum_{i \sim j} \omega_i \omega_j}{\sum_{i \sim j} |\omega_i \omega_j|}, \tag{105}$$

where the sums are over all pairs of adjacent cells, and where ω_i denotes the average signed scalar vorticity of the apparent swimming velocity in cell i:

$$\omega_i = \hat{\mathbf{z}} \cdot \int_i \nabla \times \left(\mathbf{u} + \frac{Pe_s}{c} \mathbf{m} \right). \tag{106}$$

From the above definition, we see that $\chi = 1$ if the net flow is rotating in the same direction in every single cell. On the contrary, $\chi = -1$ in a system where the direction of rotation systematically alternates between adjacent cells. Finally, we expect $\chi \approx 0$ in a system where the direction of rotation of adjacent cells is completely uncorrelated, so that a pair is equally likely to rotate in the same direction as in the opposite direction. We also define the time-averaged relative asymmetry between the populations N_+ of anticlockwise cells ($\omega_i > 0$) and N_- of clockwise cells ($\omega_i < 0$):

$$\delta = \frac{1}{t_f} \int_0^{t_f} \frac{N_+ - N_-}{N_+ + N_-}. \tag{107}$$

In a perfectly symmetric or uncorrelated system we expect $N_+ = N_-$ and therefore $\delta = 0$, whereas $\delta = \pm 1$ describes a system in which nearly all the cells are rotating in the same direction.

Snapshots from a series of simulations in lattices with increasing gap size a are shown in Fig. 11, and corresponding data for χ and δ as functions of a is plotted in Fig. 12. In the limit of vanishing gap size ($a \to 0$) the cells are disconnected and the direction of rotation in a given cell becomes independent of its neighbors ($\chi \to 0$). As the gap is enlarged, hydrodynamic stresses and transport across junctions lead to interactions between cells, first causing a positive correlation between the direction of rotation of adjacent cells ($\chi > 0$). This is the case of $a = 0.075$ and 0.1 in Fig. 11, where we measure $\chi = 0.46$ and 0.31. This positive correlation results in large steady patches of co-rotating cells, with larger values of χ corresponding to larger patch sizes. In this regime, we note that the flow in each cell is nearly identical everywhere (up to the direction of rotation), and resembles the double vortex in circular chambers (Fig. 7). As first proposed by Wioland et al. [62], who reported similar trends in their experiments, this positive correlation is consistent with the well-known tendency of swimmers to swim along boundaries. Note that Wioland et al. also reported a negative correlation in the limit of extremely small gaps, which they attributed to the inability of bacteria to enter the gaps; this regime is not seen in our simulations, which do not take finite swimmer size into account.

Increasing a beyond ≈ 0.1 causes a decrease in χ, and the positively correlated state persists for openings up to $a \approx 0.225$. For this value of a we measure $\chi = -8 \times 10^{-4}$, and inspection of the flow patterns in Fig. 11 indeed shows no evidence of correlation, with equal likelihood for a pair of adjacent cells to co- or counter-rotate. The increase in gap width is also seen to have an effect on the flow patterns: while an underlying double vortex is visible in each cell, more complex flow structures involving jets between adjacent cells and circulating flows around pillars or groups of pillars become noticeable.
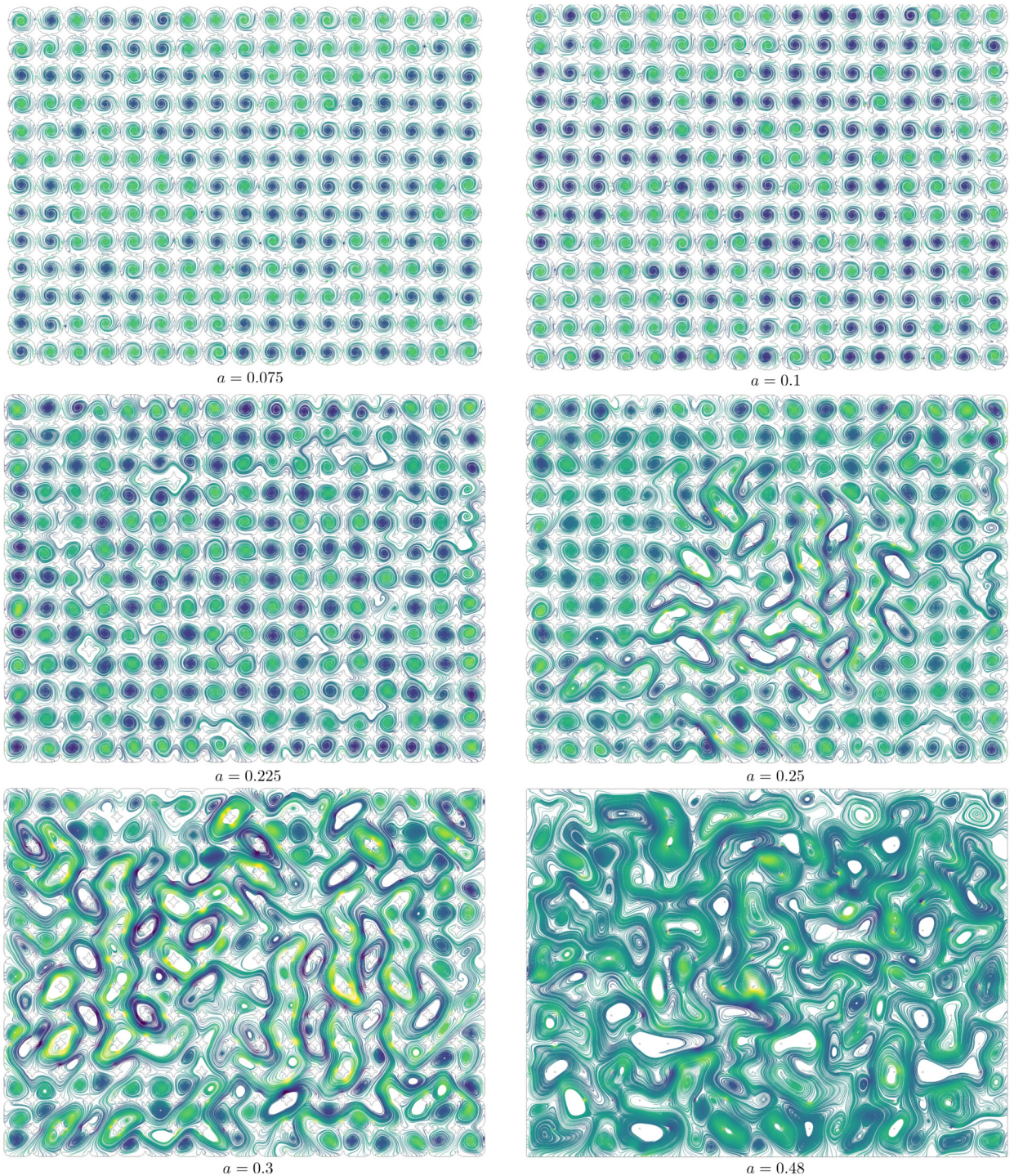
Fig. 11. Active flows in lattices: flow patterns for increasing gap opening *a*. The streamlines of the net bacterial flow are colored by vorticity, where green corresponds to clockwise rotation and blue to counterclockwise.

As the size of the junctions keeps on increasing ($a = 0.25, 0.3, 0.48$ in Fig. 11), the flow becomes systematically unsteady and increasingly more complex, with fluid jets that travel across the lattice spanning multiple cells. The emergence of these complex patterns is the result of the diminishing influence of the walls, which allows for an increasing number of unsteady modes to grow and interact in the system. In spite of the chaotic nature of the flow, vorticity remains noticeably anti-correlated between adjacent cells, as confirmed by the values of $\chi < 0$ in Fig. 12. This remains true even for the
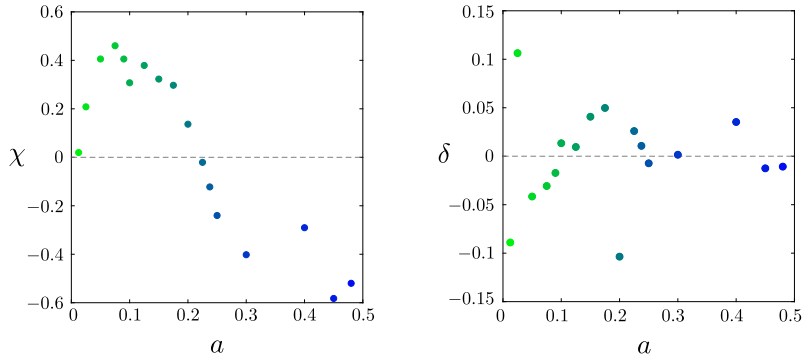
Fig. 12. Average spin-spin correlation χ defined in Eq. (105), and time-averaged relative asymmetry δ between clockwise and counterclockwise cells defined in Eq. (107).

smallest pillars ($a = 0.48$), which still set the dominant wavelength of the flow and serve to guide the bacterial jets across the lattice. The dynamics in this case is also consistent with the recent experiments of Nishiguchi et al. [41] on bacteria in pillar arrays, where similar chaotic flows were observed with a coherence length set by the lattice spacing. By simply varying a, our simulations reveal a rich variety of flow patterns and thus demonstrate the ability of judiciously designed periodic lattices to control bacterial flow on a wide range of scales, from the pore scale to the patch size.

While the spin-spin correlation χ shows clear trends with increasing gap size with a transition from positive to negative correlation, the relative asymmetry δ remains between ± 0.1 for all values of a. This suggests that clockwise/counterclockwise symmetry is essentially preserved on large length scales. Nevertheless, we note that the largest fluctuations in δ occur when $\chi \approx 0$, i.e. when the coupling between adjacent cells is the weakest, which could indicate that global symmetry is in fact favored in strongly interacting lattice flows. The fact that δ is reasonably well centered around 0 is also an indication that our numerical method does not introduce a preferred direction of rotation.

7.4. Three-dimensional simulations

In this last section, we present numerical results in three spatial dimensions, illustrating the ability of our mathematical and computational methods to be extended to 3D and opening the way for future potential exploration. The 3D computational approach follows the same numerical techniques as in 2D and shares the same accuracy, stability and adaptivity properties. The domain geometries we consider here, namely spherical cavities and periodic channels, are 3D analogs of the 2D geometries analyzed in our previous study [55].

7.4.1. Spherical cavity

For this first example, we consider the active flow in a suspension of pushers confined inside a spherical cavity of diameter 1. As for the 2D case of section 7.2, we choose

$$Pe_s = 0.5, \quad \Lambda = 0.1, \quad t_f = 5, \quad \Omega = [-1, 1]^3, \tag{108}$$

and consider three levels of activity $\alpha = -1, -20, -200$. We perform simulations on a three-dimensional Octree grid with a maximum level of 7, which contains on the order of 400,000 grid points. Each time step takes between 5 and 10 minutes using OpenMP and ten threads on a desktop computer.

The simulated flow patterns are depicted in Fig. 13. The 3D solutions show patterns that could have been anticipated from the 2D case. At low levels of activity, there is no active flow and the distribution of swimmers is radial with accumulation at the boundary accompanied by wall-normal polarization. As activity increases, a steady three-dimensional double vortex emerges spontaneously, with an axis of rotation which is selected arbitrarily by the system. Finally, 3D chaotic dynamics are observed at the highest activity level.
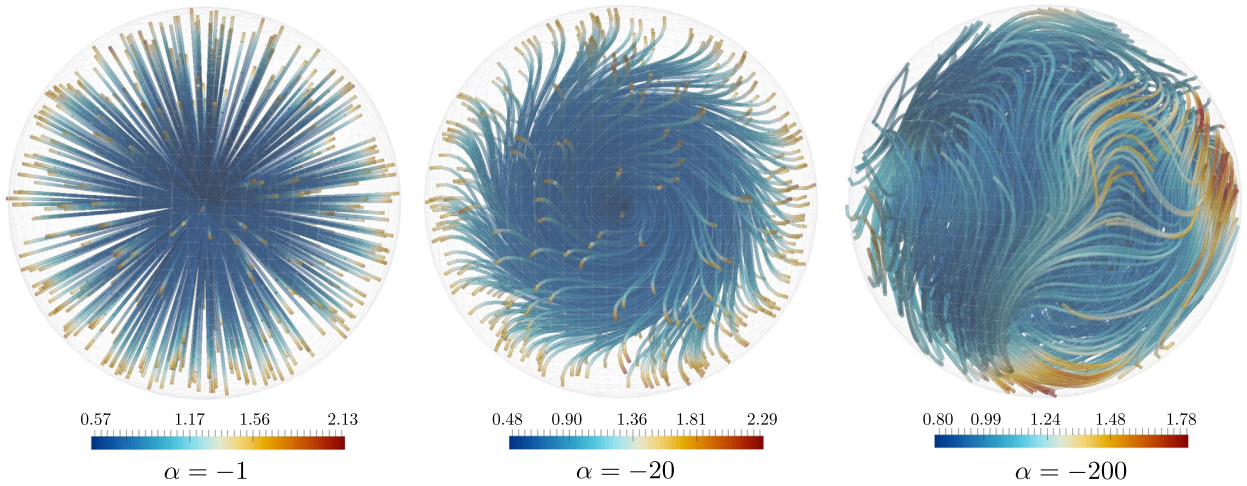
7.4.2. Torus

Next, we simulate active flows inside a periodic channel shaped as a torus with inner radius $R_{\min} = 0.5$ and width $W = 1$. The associated level set function is

$$\phi(x, y, z) = \left[\left(\sqrt{x^2 + y^2} - R_{\min} - \frac{W}{2} \right)^2 + z^2 \right]^{\frac{1}{2}} - \frac{W}{2}. \tag{109}$$

We choose the parameters as

$$Pe_s = 0.5, \quad \Lambda = 0.5, \quad t_f = 5, \quad \Omega = [-2.25, 2.25]^3, \quad \max_{\text{level}} = 7, \quad T_V = 0.02, \quad \max_V = 6, \tag{110}$$

and analyze active flows with increasing activity levels.

Fig. 13. Active flow in a pusher suspension confined inside a spherical cavity. The figure shows streamlines of the net swimmer velocity, with colors corresponding to the velocity magnitude. As in the 2D example of Fig. 7, we take $\Lambda = 0.1$, $Pe_s = 0.5$ and vary the level of activity: from left to right $\alpha = -1, -20, -200$. Simulations are performed on a Octree grid with $\max_{level} = 7$.
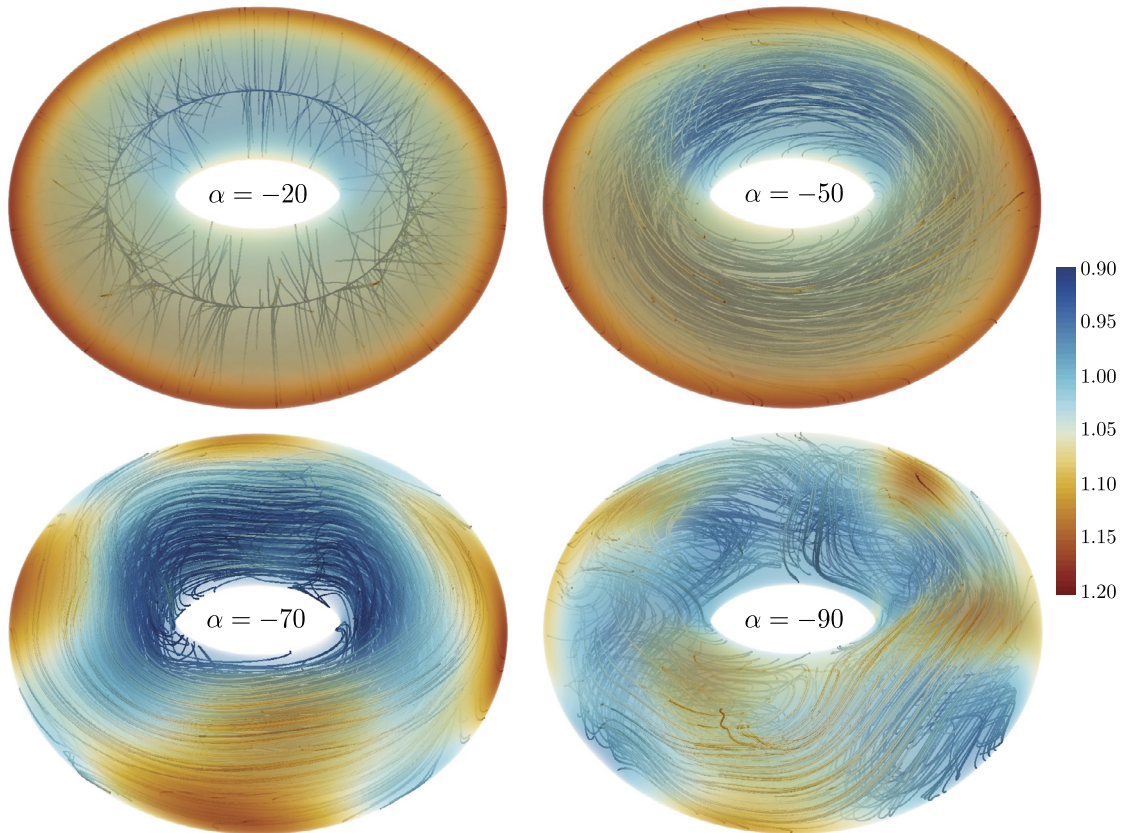
Fig. 14. Active flows inside a periodic channel shaped as a torus for increasing activity levels α. The concentration field (colors) is superimposed onto streamlines of the net swimmer velocity. From top left to bottom right: $\alpha = -20, -50, -70, -90$.

Once again, the simulated active flows resemble those observed in our previous work [55] in 2D periodic channels, with four distinct flow regimes as illustrated in Fig. 14. At low levels of activity ($\alpha = -20$), the fluid is quiescent and swimmers preferentially accumulate at the wall, aligning in the normal direction on average. As activity increases ($\alpha = -50$), a spontaneous steady flow emerges in an arbitrary direction, which is azimuthally symmetric and against which the swimmers propel. As activity is increased further ($\alpha = -70$), the steady flow persists but axisymmetry is lost and we
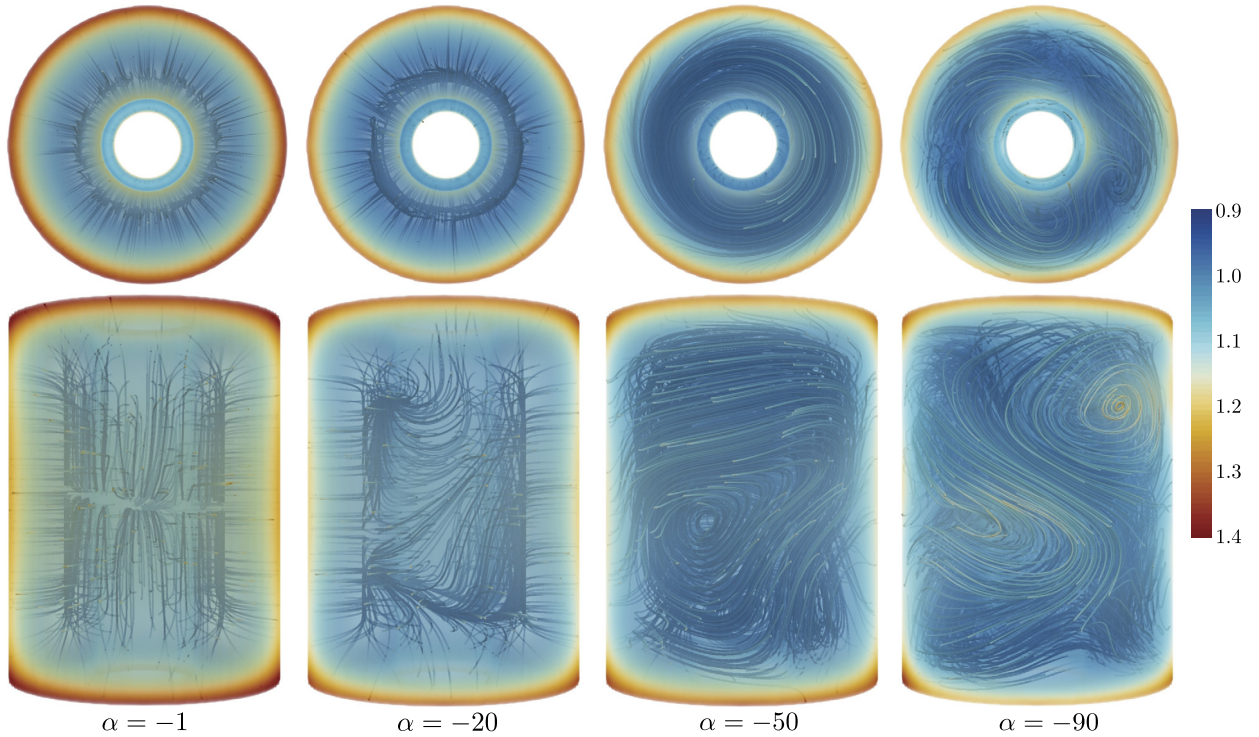
Fig. 15. Active flows in suspensions of pushers confined inside the gap between two concentric cylinders, for increasing activity levels. From left to right: $\alpha = -1, -20, -50, -90$.

observe evenly spaced clusters of swimmers that are transported as density waves. At high activity levels ($\alpha = -90$), the flow eventually destabilizes and becomes unsteady and chaotic as already observed in other geometries.

7.4.3. Concentric cylinders

As a final example, we conduct a similar analysis in another periodic domain defined as the gap between two concentric cylinders with inner radius $R_{\min} = 0.5$, gap width $W = 1$, and bounded in the axial direction with a height of $H = 4$ (see Fig. 15). The level set function for this geometry is defined as

$$\phi(x, y, z) = \max\left\{ \sqrt{x^2 + y^2} - R_{\min} - W, \; R_{\min} - \sqrt{x^2 + y^2}, \; |z| - \frac{H}{2} \right\}. \tag{111}$$

All other physical and computational parameters ($Pe_s, \Lambda, t_f, \Omega, \max_{\text{level}}, T_V, \max_V$) are chosen as in Eq. (110).

Typical flow patterns and concentration fields are shown in Fig. 15 for $\alpha = -20, -50, -70, -90$. Similar flow transitions as in previous geometries occur. In weakly active systems, swimmers simply accumulate at the walls, and do not drive any net flow. Interestingly, we find that accumulation is maximum at corners, in agreement with experimental observations [16]. Upon increasing $|\alpha|$, a transition to a flowing state is observed, which is primarily azimuthal with some vertical fluctuations. This ultimately leads to chaotic dynamics in strongly active systems. A key difference with the flows observed in the torus in section 7.4.2 can be noted: the sizeable height of the domain indeed allows for significant unsteady motions in the z direction, which are superimposed onto the net azimuthal flow and likely play a role in its destabilization. These observations are consistent with experiments on microtubule/kinesin cluster solutions in a similar geometry [65], which have shown a subtle dependence on channel aspect ratio with a disruption of azimuthal flow in tall channels. The spontaneous emergence of azimuthal flow in this geometry also underlies rheological measurements on bacterial suspensions in circular Couette cells [29], which report a net angular velocity at zero torque in sufficiently concentrated systems.

8. Conclusion

We have presented a novel numerical approach for the efficient simulation of the dynamics of active fluids in various confined microfluidic geometries. Our simulations are based on a mean-field continuum model for suspensions of microswimmers such as bacteria or self-propelled colloids, which consists of coupled advection-diffusion equations for the swimmer concentration, polarization, and nematic tensor along with the forced Navier-Stokes equations for the fluid flow induced by internal active stresses. The difficulty in simulating this system in complex geometries stems from the importance

of accurately resolving microstructural variables in the vicinity of boundaries, where swimmers are known to accumulate, while also capturing unsteady flow features in the bulk fluid. As a result, most prior simulations have been limited to two dimensions and simple geometries, and our approach takes a major step towards extending our understanding of active fluid flows to complex three-dimensional systems.

The versatility of our method hinges on the use of level sets to represent complex domain shapes, along with adaptively refined Quad-/Octree grids that are ideally suited for capturing the wide range of scales present in the system. A novel hybrid spatial discretization was also introduced, which employs finite volumes for the concentration field so as to ensure mass conservation, while using a combination of finite volumes and finite differences for the polarization and nematic fields, which provides enhanced accuracy while easily satisfying Neumann boundary conditions at the walls. Finally, an unconditionally stable projection solver for the incompressible Navier-Stokes equations developed in previous work was adopted for the active fluid flow.

We illustrated our approach by analyzing spontaneous active flows in a variety of microfluidic geometries in both two and three dimensions, which were inspired by recent experiments on bacterial suspensions. Our results were all consistent with experimental observations and demonstrated the ability of our model to capture subtle features such as wall accumulation layers, spontaneous flow transitions, double vortices, and large-scale synchronization. While a complete characterization of active fluid dynamics in arbitrary geometries remains to be done, these results highlight the potential of our framework to be applied towards this goal. The efficiency of our approach also makes it an ideal choice for design applications relying on shape optimization. Our method can also easily be extended to model other types of active matter systems, such as active nematic gels [33], or to account for other physical effects such as chemotaxis [13,31], externally applied fields [2] or imposed flows [1].

Acknowledgements

References

[1] A. Alizadeh Pahlavan, D. Saintillan, Instability regimes in flowing suspensions of swimming micro-organisms, Phys. Fluids 23 (2011) 011901.
[2] R. Alonso-Matilla, D. Saintillan, Microfluidic flow actuation using magnetoactive suspensions, Europhys. Lett. 121 (2018) 24002.
[3] T. Aslam, A partial differential equation approach to multidimensional extrapolation, J. Comput. Phys. 193 (2004) 349–355.
[4] A. Baskaran, M.C. Marchetti, Statistical mechanics and hydrodynamics of bacterial suspensions, Proc. Natl. Acad. Sci. USA 106 (2009) 15567–15572.
[5] F.P. Bretherton, The motion of rigid particles in a shear flow at low Reynolds number, J. Fluid Mech. 14 (1962) 284–304.
[6] S. Chen, P. Gao, T. Gao, Dynamics and structure of an apolar active suspension in annulus, J. Fluid Mech. 835 (2018) 393–405.
[7] C. Cleret de Langavant, A. Guittet, M. Theillard, F. Temprano-Coleto, F. Gibou, Level-set simulations of soluble surfactant driven flows, J. Comput. Phys. 348 (2017) 271–297.
[8] K. Drescher, J. Dunkel, L.H. Cisneros, S. Ganguly, R.E. Goldstein, Fluid dynamics and noise in bacterial cell-cell and cell-surface scattering, Proc. Natl. Acad. Sci. USA 108 (2011) 10940–10945.
[9] K. Drescher, R.E. Goldstein, N. Michel, M. Polin, I. Tuval, Direct measurement of the flow field around swimming microorganisms, Phys. Rev. Lett. 105 (2010) 168101.
[10] J. Elgeti, G. Gompper, Wall accumulation of self-propelled spheres, Europhys. Lett. 101 (2013) 48003.
[11] J. Elgeti, G. Gompper, Run-and-tumble dynamics of self-propelled particles in confinement, Europhys. Lett. 109 (2015) 58003.
[12] A.A. Evans, T. Ishikawa, T. Yamaguchi, E. Lauga, Instabilities and global order in concentrated suspensions of spherical microswimmers, Phys. Fluids 23 (2011) 111702.
[13] B. Ezhilan, A. Alizadeh Pahlavan, D. Saintillan, Chaotic dynamics and oxygen transport in thin films of aerotactic bacteria, Phys. Fluids 24 (2012) 091701.
[14] B. Ezhilan, D. Saintillan, Transport and rheology of a dilute active suspension in pressure-driven channel flow, J. Fluid Mech. 777 (2015) 482–522.
[15] B. Ezhilan, M.J. Shelley, D. Saintillan, Instabilities and nonlinear dynamics of concentrated active suspensions, Phys. Fluids 25 (2013) 070607.
[16] N. Figueroa-Morales, G.L. Miño, A. Rivera, R. Caballero, E. Clément, E. Altshuler, A. Lindner, Living on the edge: transfer and traffic of *E. coli* in a confined flow, Soft Matter 11 (2015) 6284–6393.
[17] T. Gao, M. Betterton, A. Huang, M. Shelley, Analytical structure, dynamics, and reduction of a kinetic model of an active fluid, Phys. Rev. Fluids 2 (2017) 093302.
[18] T. Gao, R. Blackwell, M. Glaser, D. Betterton, M. Shelley, Multiscale modeling and simulation of microtubule/motor-protein assemblies, Phys. Rev. E 92 (2015) 062709.
[19] A. Guittet, M. Theillard, F.F. Gibou, A stable projection method for the incompressible Navier-Stokes equations on arbitrary geometries and adaptive quad/octrees, J. Comput. Phys. 292 (2015) 215–238.
[20] Y. Hatwalne, S. Ramaswamy, M. Rao, R. Aditi Simha, Rheology of active-particle suspensions, Phys. Rev. Lett. 92 (2004) 118101.
[21] J.P. Hernandez-Ortiz, C.G. Stoltz, M.D. Graham, Transport and collective dynamics in suspensions of confined swimming particles, Phys. Rev. Lett. 95 (2005) 204501.
[22] C. Hohenegger, M. Shelley, Stability of active suspensions, Phys. Rev. E 81 (2010) 046311.
[23] G.B. Jeffery, The motion of ellipsoidal particles immersed in a viscous fluid, Proc. R. Soc. Lond. A 102 (1922) 161–179.
[24] D.L. Koch, G. Subramanian, Hydrodynamics of swimming microorganisms: living fluids, Annu. Rev. Fluid Mech. 43 (2011) 637–659.
[25] E. Lauga, T.R. Powers, The hydrodynamics of swimming microorganisms, Rep. Prog. Phys. 72 (2009) 096601.
[26] C.F. Lee, Active particles under confinement: aggregation at the wall and gradient formation inside a channel, New J. Phys. 15 (2013) 055007.
[27] G. Li, J. Bensson, L. Nisimova, D. Munger, P. Mahautmr, J.X. Tang, M.R. Maxey, Y.V. Brun, Accumulation of swimming bacteria near a solid surface, Phys. Rev. E 84 (2011) 041932.

[28] G. Li, J.X. Tang, Accumulation of microswimmers near a surface mediated by collision and rotational Brownian motion, Phys. Rev. Lett. 103 (2009) 078101.

[29] H.M. López, J. Gachelin, C. Douarche, H. Auradou, E. Clément, Turning bacteria suspensions into superfluids, Phys. Rev. Lett. 115 (2015) 028301.

[30] F. Losasso, F. Gibou, R. Fedkiw, Simulating water and smoke with an octree data structure, ACM Trans. Graph. (SIGGRAPH Proc.) (2004) 457–462.

[31] E. Lushi, R.E. Goldstein, M.J. Shelley, Nonlinear concentration patterns and bands in autochemotactic suspensions, Phys. Rev. E 98 (2018) 052411.

[32] E. Lushi, H. Wioland, R.E. Goldstein, Fluid flows created by swimming bacteria drive self-organization in confined suspensions, Proc. Natl. Acad. Sci. USA 111 (2014) 9733–9738.

[33] M.C. Marchetti, J.F. Joanny, S. Ramaswamy, T.B. Liverpool, J. Prost, M. Rao, R. Aditi Simha, Soft active matter, Rev. Mod. Phys. 85 (2013) 1143–1189.

[34] C. Min, F. Gibou, A second order accurate projection method for the incompressible Navier-Stokes equation on non-graded adaptive grids, J. Comput. Phys. 219 (2006) 912–929.

[35] C. Min, F. Gibou, Geometric integration over irregular domains with application to level set methods, J. Comput. Phys. 226 (2007) 1432–1443.

[36] C. Min, F. Gibou, A second order accurate level set method on non-graded adaptive Cartesian grids, J. Comput. Phys. 225 (2007) 300–321.

[37] C. Min, F. Gibou, H. Ceniceros, A supra-convergent finite difference scheme for the variable coefficient Poisson equation on non-graded grids, J. Comput. Phys. 218 (2006) 123–140.

[38] M. Mirzadeh, M. Theillard, F. Gibou, A second-order discretization of the nonlinear Poisson-Boltzmann equation over irregular geometries using non-graded adaptive Cartesian grids, J. Comput. Phys. 230 (2011) 2125–2140.

[39] M. Mirzadeh, M. Theillard, A. Helgadóttir, D. Boy, F. Gibou, An adaptive, finite difference solver for the nonlinear Poisson-Boltzmann equation with applications to biomolecular computations, Commun. Comput. Phys. 13 (2013) 150–173.

[40] J.L. Moran, J.D. Posner, Phoretic self-propulsion, Annu. Rev. Fluid Mech. 49 (2017) 511–540.

[41] D. Nishiguchi, I.S. Aranson, A. Snezhko, A. Sokolov, Engineering bacterial vortex lattice via direct laser lithography, Nat. Commun. 9 (2018) 4486.

[42] S. Osher, J.A. Sethian, Fronts propagating with curvature-dependent speed: algorithms based on Hamilton-Jacobi formulations, J. Comput. Phys. 79 (1988) 12–49.

[43] L. Rothschild, Non-random distribution of bull spermatozoa in a drop of sperm suspension, Nature 198 (1963) 1221–1222.

[44] D. Saintillan, The dilute rheology of swimming suspensions: a simple kinetic model, Exp. Mech. 50 (2010) 1275–1281.

[45] D. Saintillan, Rheology of active fluids, Annu. Rev. Fluid Mech. 50 (2018) 563–592.

[46] D. Saintillan, M. Shelley, Emergence of coherent structures and large-scale flows in motile suspensions, J. R. Soc. Interface 9 (2012) 571–585.

[47] D. Saintillan, M.J. Shelley, Orientational order and instabilities in suspensions of self-locomoting rods, Phys. Rev. Lett. 99 (2007) 058102.

[48] D. Saintillan, M.J. Shelley, Instabilities and pattern formation in active particle suspensions: kinetic theory and continuum particle simulations, Phys. Rev. Lett. 100 (2008) 178103.

[49] D. Saintillan, M.J. Shelley, Instabilities, pattern formation and mixing in active suspensions, Phys. Fluids 20 (2008) 123304.

[50] D. Saintillan, M.J. Shelley, Active suspensions and their nonlinear models, C. R. Phys. 14 (2013) 497–517.

[51] H. Samet, Applications of Spatial Data Structures: Computer Graphics, Image Processing and GIS, Addison-Wesley, New York, 1990.

[52] T. Sanchez, D. Chen, S. DeCamp, M. Heymann, Z. Dogic, Spontaneous motion in hierarchically assembled active matter, Nature 491 (2012) 431–434.

[53] M.J. Shelley, The dynamics of microtubule/motor-protein assemblies in biology and physics, Annu. Rev. Fluid Mech. 48 (2016) 487–506.

[54] G. Subramanian, D.L. Koch, Critical bacterial concentration for the onset of collective swimming, J. Fluid Mech. 632 (2009) 359–400.

[55] M. Theillard, R. Alonso-Matilla, D. Saintillan, Geometric control of active collective motion, Soft Matter 13 (2017) 363–375.

[56] M. Theillard, L.F. Djodom, J.-L. Vié, F. Gibou, A second-order sharp numerical method for solving the linear elasticity equations on irregular domains and adaptive grids—application to shape optimization, J. Comput. Phys. 233 (2013) 430–448.

[57] M. Theillard, F. Gibou, T. Pollock, A sharp computational method for the simulation of the solidification of binary alloys, J. Sci. Comput. 63 (2015) 330–354.

[58] M. Theillard, C. Rycroft, F. Gibou, A multigrid method on non-graded adaptive Octree and Quadtree Cartesian grids, J. Sci. Comput. 55 (2013) 1–15.

[59] R. Voituriez, J.F. Joanny, J. Prost, Spontaneous flow transition in active polar gels, Europhys. Lett. 70 (2005) 404–410.

[60] H.H. Wensink, J. Dunkel, S. Heidenreich, K. Drescher, R.E. Goldstein, H. Löwen, J.M. Yeomans, Meso-scale turbulence in living fluids, Proc. Natl. Acad. Sci. USA 109 (2012) 14308–14313.

[61] H. Wioland, E. Lushi, R.E. Goldstein, Directed collective motion of bacterial under channel confinement, New J. Phys. 18 (2015) 075002.

[62] H. Wioland, F.G. Woodhouse, J. Dunkel, R.E. Goldstein, Ferromagnetic and antiferromagnetic order in bacterial vortex lattices, Nat. Phys. 12 (2016) 341–345.

[63] H. Wioland, F.G. Woodhouse, J. Dunkel, J.O. Kessler, R.E. Goldstein, Confinement stabilizes a bacterial suspension into a spiral vortex, Phys. Rev. Lett. 110 (2013) 268102.

[64] F.G. Woodhouse, R.E. Goldstein, Spontaneous circulation of confined active suspensions, Phys. Rev. Lett. 109 (2012) 168105.

[65] K.T. Wu, J.B. Hishamunda, D.T.N. Chen, S.J. DeCamp, Y.W. Chang, A. Fernández-Nieves, S. Fraden, Z. Dogic, Transition from turbulent to coherent flows in confined three-dimensional active fluids, Science 355 (2017) eaal1979.